Instabilities in Stagnation Point Flows of Polymer Solutions

S. J. Haward[1,2,a)] and G. H. McKinley[1]

[1] *Hatsopoulos Microfluids Laboratory, Department of Mechanical Engineering, Massachusetts Institute of Technology, Cambridge, MA 02139, USA*

[2] *Faculdade de Engenharia da Universidade do Porto, Centro de Estudos de Fenómenos de Transporte, Rua Dr. Roberto Frias, 4200-465, Porto, Portugal*

A recently-developed microfluidic device, the optimized shape cross-slot extensional rheometer, or OSCER [S.J. Haward, M.S.N. Oliveira, M.A. Alves and G.H. McKinley, Phys. Rev. Lett. **109**, 128301 (2012)], is used to investigate the stability of viscoelastic polymer solutions in an idealized planar stagnation point flow. Aqueous polymer solutions, consisting of poly(ethylene oxide) and of hyaluronic acid with various molecular weights and concentrations, are formulated in order to provide fluids with a wide range of rheological properties. Semi-dilute solutions of high molecular weight polymers provide highly viscoelastic fluids with long relaxation times, which achieve a high Weissenberg number (Wi) at flow rates for which the Reynolds number (Re) remains low; hence the elasticity number El = Wi/Re is high. Lower concentration solutions of moderate molecular weight polymers provide only weakly viscoelastic fluids in which inertia remains important and El is relatively low. Flow birefringence observations are used to visualize the nature of flow instabilities in the fluids as the volume flow rate through the OSCER device is steadily incremented. At low Wi and Re, all of the fluids display a steady, symmetric and uniform 'birefringent strand' of highly oriented polymer molecules aligned along the outflowing symmetry axis of the test geometry, indicating the stability of the flow field under such conditions. In fluids of El > 1, we observe steady elastic flow asymmetries beyond a critical Weissenberg number, Wi_{crit}, that are similar in character to those already reported in standard cross-slot geometries [e.g. P.E. Arratia, C.C. Thomas, J. Diorio and J.P. Gollub, Phys. Rev. Lett. **96**, 144502 (2006)]. However, in fluids with El < 1 we observe a sequence of time-dependent inertio-elastic instabilities beyond a critical Reynolds number, Re_{crit}, characterized by high frequency spatiotemporal oscillations of the birefringent strand. By plotting the critical limits of stability for the various fluids in the Wi-Re operating space, we are able to construct a stability diagram delineating the distinct steady symmetric, steady asymmetric and inertio-elastic flow regimes in this idealized planar elongational flow device.

[a)] Author to whom correspondence should be addressed. Tel.: +351 225081404. FAX: +351 225081449. Electronic mail: shaward@fe.up.pt

I. INTRODUCTION

Extensional flows arise wherever there is a velocity gradient aligned with the direction of fluid flow and typically occur in geometries such as contractions, bifurcations, at the trailing stagnation points of obstacles and sedimenting objects as well as in the necking and breakup of fluid jets and drops. In extensional flows of polymer solutions, when the velocity gradient (or strain rate, $\dot{\varepsilon}$) exceeds one-half of the relaxation rate of the polymer ($0.5/\lambda$, where λ is the characteristic relaxation time), such that the Weissenberg number $\mathrm{Wi} = \lambda\dot{\varepsilon} > 0.5$, macromolecules can be significantly deformed from their equilibrium Gaussian coiled conformation,[1-3] leading to orders-of-magnitude increases in the apparent extensional viscosity of the fluid, even for dilute solutions.[4-6] It is this strain hardening property that is exploited in numerous industrial and biological processes and applications, ranging from enhanced oil recovery, inkjet printing, turbulent drag reduction and fiber-spinning, to flows of mucin secretions and polysaccharide solutions in the circulatory systems of animals. The extensional viscosity is recognized as a fundamental material function that must be quantified in order to fully characterize the rheology of complex fluids. However, it is a very challenging property to measure accurately, in large part because of its dependence on both the imposed strain rate and the total applied fluid strain, and also due to the difficulty involved in generating a shear-free homogeneous extensional flow field.[7] There are further experimental challenges associated with measuring the extensional viscosity of weakly strain hardening and low viscosity fluids due to the difficulty in achieving a sufficient strain rate to probe elastic effects at high Wi while simultaneously minimizing fluid inertia.

Recently, we presented a new microfluidic device called the Optimized Shape Cross-Slot Extensional Rheometer (OSCER, Fig. 1).[8] The OSCER device is based upon the planar cross-slot geometry, with incoming flow through the two opposing vertical channels and flow out of the two diametrically-opposed horizontal channels. Assuming symmetry of the flow field, this configuration results in a free stagnation point at the center of the OSCER device. The OSCER geometry has been numerically optimized[9,10] in order to provide a homogeneous extensional flow field over a length $15H$ either side of the stagnation point, where H = 100 μm is the characteristic channel half-width up and downstream of the central, optimized region. The channel generates a quasi-two-dimensional flow field due to its large depth, d = 2.1 mm and high

aspect ratio $\alpha = d/2H = 10.5$. Streamlines near the center of the OSCER device closely approximate hyperbolae, with a singular hyperbolic point occurring in the precise center of the device (the stagnation point). Here the flow velocity is zero, but the strain rate is still finite, and the long residence time of fluid elements in this locality results in the accumulation of very high fluid strains. When the Weissenberg number is high (i.e. Wi > 0.5), polymeric macromolecules that are present in such fluid elements are also subjected to the high strains that are required to observe the steady-state limiting value of the extensional viscosity. It has been experimentally demonstrated by measurements of flow-induced birefringence (FIB) and also by direct observations of fluorescently-labeled DNA, that polymer molecules trapped in the vicinity of stagnation points can undergo a coil-stretch transition and approach an almost fully-stretched state.[11-15] In FIB experiments within the OSCER device (as within conventional cross-slots), a sharply localized birefringent strand can be observed along the outflowing symmetry plane for Wi > 0.5, indicating the development of significant optical anisotropy among macromolecules that pass near the stagnation point.[8,10,16] Moreover, along the symmetry planes of the OSCER device (the $x = 0$ and $y = 0$ planes) there is zero shear, and hence the flow field in these regions provides a purely planar extensional deformation to fluid elements. The OSCER device therefore largely satisfies the requirements to be considered as a true extensional rheometer, and we have already demonstrated its use as such in a number of recent publications.[8,10,16]

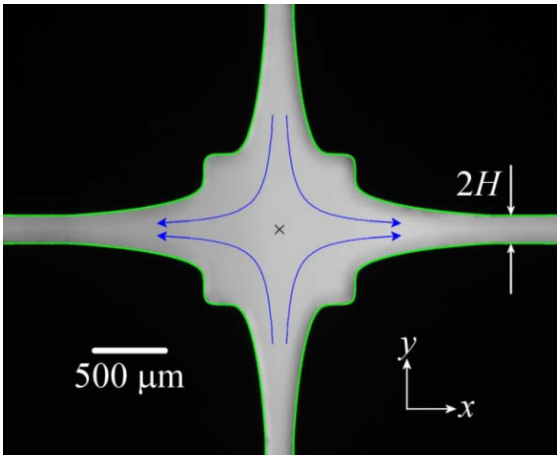

FIG. 1. Photograph of the OSCER geometry with the ideal profile superimposed in green. Flow enters through the vertical channels (y-direction) and exits through the horizontal channels (x-direction). Streamlines closely follow hyperbolae within the central region of the device and generate a stagnation point at the center of the device (marked by the cross). The characteristic channel dimension is H = 100 μm and the (uniform) device depth is d = 2.1 mm.

The strain rate in the OSCER device is set by controlling the superficial flow velocity ($U = Q/4Hd$, where Q is the total volume flow rate through the device), which results in a nominal imposed extensional strain rate $\dot{\varepsilon} \approx 0.1U/H$.[8,10] In microfluidic devices, such as the OSCER, the small length scale H allows access to very high strain rates, hence elastic effects (as characterized by the magnitude of the Weissenberg number $\mathrm{Wi} = \lambda\dot{\varepsilon}$) can be large even for fluids with short relaxation times. On the other hand, the small length scale also means that inertial effects, as characterized by the Reynolds number (defined as either $\mathrm{Re} = \rho UH/\eta$ or $\mathrm{Re} = \rho UD_h/\eta$, where $D_h = 4dH/(2H + d)$ is the hydraulic diameter and ρ and η are the fluid density and viscosity, respectively) can be kept relatively low. An *elasticity number* characterizing the relative importance of elastic to inertial effects can be defined as $\mathrm{El} = \mathrm{Wi}/\mathrm{Re} \sim \lambda\eta/\rho H^2$. Thus it is apparent that the small length scale of the OSCER device allows elastic effects to be observed even in weakly elastic, low viscosity fluids. Hence the device can be used to characterize the extensional rheological properties of fluids such as dilute aqueous polymer solutions, which pose a major challenge for any currently available commercial instruments.[17]

As with all rheometers, the OSCER also has an upper operating bound, which originates primarily from the onset of flow instabilities that occur as the flow rate is incremented beyond (fluid-dependent) critical conditions. In Newtonian fluids, it is well known that flow instabilities arise as the flow rate is increased due to the effect of fluid inertia. However, in viscoelastic fluids instabilities can also arise as the Weissenberg number, Wi, becomes high, even though the Reynolds number may remain extremely low.[18,19]

Flow instabilities in viscoelastic fluids are interesting dynamical phenomena and have potential applications in microfluidic devices where they can be utilized in flow control elements such as switches and diodes,[20,21] or exploited to produce efficient mixing at low Reynolds numbers.[22] In recent years considerable effort has been invested in trying to characterize and understand the "purely-elastic" flow instabilities that are observed at low Reynolds number in strong extensional flows of viscoelastic fluids in microfluidic capillary entrance flows[23-29] and also in conventionally shaped cross-slot devices.[30-36] Using a microfluidic cross-slot geometry, Arratia *et al*.[30] observed a purely elastic symmetry-breaking flow bifurcation, which occurred in

a dilute polyacrylamide solution as the Weissenberg number exceeded a critical value of $\mathrm{Wi}_{crit} \approx 4.5$, even though the Reynolds number remained $\mathrm{Re} < 10^{-2}$. In these experiments, the flow field bifurcated and developed a steady asymmetry in which the majority of fluid entering through each opposing inlet channel exited preferentially through one or other of the two outlet channels (rather than dividing symmetrically between them). At much higher $\mathrm{Wi} > 12.5$ the flow became unsteady and time dependent (though the Reynolds number still remained $\mathrm{Re} < 10^{-2}$). Similar results were later reproduced by Poole *et al*.[32] and Rocha *et al*.[33] in full-field flow simulations using a range of nonlinear viscoelastic constitutive models. Closely related phenomena have also been observed in cross-slot flows of viscoelastic wormlike micellar solutions, in this case at vanishingly small Re.[31,35-37]

Poole *et al*.[32] have advocated a buckling mechanism as the driving force behind the steady flow bifurcation, resulting from the compressive flow between the two inlet channels of the cross-slot. However, the work of Xi and Graham[34] using a finitely extendible non-linear elastic (FENE) dumbbell model, clearly indicates that the stretching of macromolecules along the outflowing direction can also drive the onset of an oscillatory flow instability even in the absence of inertia. By looking at the effect of the dumbbell stretch on the local velocity field, Xi and Graham[34] showed that interactions between extensional stress growth and the local flow kinematics could lead to periodic oscillations in this planar elongational flow at sufficiently high Weissenberg number. We note that similar arguments were previously put forward by Harris and Rallison[38] and Harlen *et al*.[39,40] to explain the birefringent pipe structures and varicose instabilities observed in early axisymmetric stagnation point flows of polymer solutions in the opposed jets apparatus.[41-43] However, there are two important points to be aware of with regard to these early works: 1) the experimental studies were performed under conditions of very high Reynolds number ($\mathrm{Re} \sim O(10^3)$) and consequently very low El, and 2) the simulations imposed symmetry on the flow field by only modeling one-quarter of the geometry, so could not possibly have resolved the kind of steady flow asymmetries later reported by Arratia *et al* and others.[30-33,35-37] The recent full-field numerical studies have mainly been performed under inertialess ($\mathrm{Re} = 0,\ \mathrm{El} \to \infty$) conditions,[34,33] although Poole *et al*.[32] reported that up to moderate Re = 5, inertia had only a minor effect on the instability, merely delaying the flow bifurcation until a higher Wi_{crit}.

Aside from the elasticity number, another parameter that may be of importance is the *viscosity ratio*, $\beta = \eta_s / \eta_0$, where η_s is the solvent viscosity and η_0 is the zero-shear viscosity of the polymer solution. In most of the numerical simulations β is set close to unity (as appropriate for a dilute polymer solution),[32,34] which implies the fluid is non-shear-thinning. Rocha *et al*.[33] used a FENE-P model and showed that reducing β (which is equivalent to increasing the polymer concentration, or increasing the extent of shear-thinning in the fluid rheological properties) could result in a reduction of the critical Weissenberg number, Wi_{crit}, for the onset of the flow bifuraction. Rocha *et al*. also investigated the effect of the molecular *extensibility parameter*, L^2, on the conditions for flow bifurcation and found that Wi_{crit} is reduced as L^2 is increased. With the exception of the work of Arratia *et al*.,[30] the fluids that have exhibited strong elastic asymmetries in recent microfluidic-based stagnation point experiments have been highly viscous, elastic and shear-thinning (i.e. very high El, very low β) wormlike micellar solutions of poorly-defined extensibility.[31,35-37]

In this study we examine the critical onset conditions for viscoelastic flow instabilities in polymer solutions using the ideal planar extensional flow field generated within the OSCER device. We employ a wide range of complex fluids formulated from different polymers of various molecular weights and concentrations in aqueous solution to provide fluids with a very wide range of viscoelastic properties, as characterized by the elasticity number, viscosity ratio and extensibility parameter. We report detailed experimental observations of purely-elastic and inertio-elastic flow instabilities in planar extensional flows of these fluids, as manifested by the appearance of the pronounced flow-induced birefringent strands that are generated due to the strong extensional flow field and high residence times near the stagnation point. By plotting the critical conditions for the onset of flow instability in Weissenberg-Reynolds number space, we produce a prototypical stability map for polymer solutions in stagnation point flows and map the operating space for the OSCER device as an extensional rheometer for complex fluids in general.

II. EXPERIMENTAL

A. Test fluids

In order to span a wide region of Wi-Re space in the OSCER device, fluids with a wide range of elasticity number are formulated. Firstly, we employ a set of three semi-dilute aqueous solutions of poly(ethylene oxide) (PEO, Sigma Aldrich) of molecular weight $M_w = 2 \times 10^6$ g mol^{-1} prepared at a concentration of c = 0.3 wt %. We refer to these fluids as PEO2 solutions. In this case the elasticity number is varied by adding 0 wt %, 46 wt % and 66 wt % glycerol to the solvent in order to vary the solvent viscosity over the range $1 \le \eta_s \le 13$ mPa s. As η_s increases, the polymer relaxation time (λ) also increases, so a given applied strain rate $\dot{\varepsilon}$ results in a higher value of $\mathrm{Wi} = \lambda\dot{\varepsilon}$ for a lower Reynolds number, and hence a significantly higher elasticity number. Simultaneously, the polymer solute provides a relatively greater contribution to the overall magnitude of the shear viscosity of the solution (which can be represented as $\eta_0 = \eta_s + \eta_p(c)$, where η_p is the concentration-dependent polymer viscosity contribution); consequently the value of the solvent viscosity ratio $\beta = \eta_s/\eta_0$ also declines. The steady shear rheology of the PEO2 test solutions has been measured in a stress-controlled AR-G2 cone-and-plate rheometer and also in an m-VROC microchannel rheometer (Rheosense Inc., San Ramon, CA)[44] in order to access shear rates up to $\dot{\gamma} \approx 5000$ s^{-1}, see Fig. 2(a). We use the intrinsic viscosities $[\eta]$ of the PEO solutions, as reported by Rodd *et al.*,[24] in order to estimate their overlap concentrations, $c^* \approx 1/[\eta]$. From this we estimate a radius of gyration, R_g, using $c^* = 3M_w/4\pi N_A R_g^3$, where N_A is Avogadro's number.[45] In the case of the purely aqueous solvent (i.e. 0 wt % glycerol) we obtain $c^* \approx 0.1$ wt.% and $R_g \approx 93$ nm; this is in good agreement with the light-scattering results of Devanand and Selser,[46] from which we obtain $R_g \approx 101$ nm. As the concentration of glycerol in the solvent is increased, the solvent quality becomes poorer and R_g gets smaller,[24] resulting in a lower intrinsic viscosity and a higher value of c^*. The contour length, L_c, of the 2×10^6 g mol^{-1} molecules in the PEO2 solutions remains constant, however, at an estimated value of $L_c = M_w l_0/m_0 \approx 13.2$ μm, where m_0 = 42 g mol^{-1} and l_0 = 0.278 nm are the repeat unit mass and length, respectively.[47] We calculate the dimensionless

FENE extensibility parameter as $L^2 = L_c^2 \big/ \left\langle r_0^2 \right\rangle$, where $\left\langle r_0^2 \right\rangle = 6R_g^2$ is the mean-squared end-to-end separation of polymer chains in their equilibrium Gaussian coiled conformation. The resulting parameter estimates for the PEO2 solutions are listed in Table I. The relaxation times of the PEO2 solutions were measured using a capillary breakup extensional rheometer (CaBER, Cambridge Polymer Group).[48]

In addition to the PEO2 solutions, a series of semi-dilute aqueous solutions of the polysaccharide hyaluronic acid (HA) are utilized. In this case the solvent viscosity is kept constant throughout and the elasticity number is varied in two ways: 1) by varying the HA molecular weight and 2) by varying the HA concentration, both of which result in changes to the fluid viscosity and relaxation time. Two bacterial HA samples were obtained: the first (referred to as HA1.6) has a molecular weight of M_w = 1.63 × 10^6 g mol^{-1} and was obtained from Sigma Aldrich; the second (referred to as HA2.6) has a molecular weight of M_w = 2.59 × 10^6 g mol^{-1} and was obtained from Lifecore Biomedical LLC, Chaska, MN. Both samples are dissolved in phosphate-buffered saline (PBS, 0.01 M, pH 7.4, Sigma Aldrich) at concentrations of c = 0.1 wt % and c = 0.3 wt %. As shown by the flow curves in Fig. 2(b), these fluids can be strongly shear-thinning in steady shear flow, especially at higher molecular weights and concentrations. The repeat unit length and mass of HA are l_0 = 0.95 nm and $m_0 \approx 400$ g mol^{-1}, yielding $L_c \approx 3.9$ μm and $L_c \approx 6.2$ μm for the HA1.6 and HA2.6 molecules, respectively.[49] Here we estimate R_g and hence the values of c^*, $\left\langle r_0^2 \right\rangle$ and L^2 using the light scattering data of Meyer *et al.*,[50] and the results are provided in Table I. Note that for a given molecular weight, the extensibility of HA is much lower than that of PEO. This is partly due to the large mass of the disaccharide HA repeat unit and the inherent rigidity it confers to the HA backbone structure, and also because HA is a polyelectrolyte with a rather expanded coil size under equilibrium conditions. For the HA solutions the relaxation times are determined directly from flow-induced birefringence measurements made in the OSCER device, as described by Haward *et al.*[16] These values are in good agreement with those made on similar solutions in a CaBER device.[51]

In Table I we also include the details of the dilute polymer solution studied by Haward *et al.*[8] This is a non-shear-thinning dilute solution (c = 0.05 wt %, $c/c^* \approx 0.2$) of a lower molecular weight PEO (M_w = 1 × 10^6 g mol^{-1}, Sigma Aldrich) which we refer to as PEO1.

Note that in order to provide an indication of the elasticity numbers of the fluids in Table I, we define a value $El_{0.5}$, which is the elasticity number determined at a Weissenberg number of 0.5. The reason for adopting this convention is because, in general, most of the fluids are quite strongly shear-thinning, so the elasticity number is not constant but is a function of the imposed flow rate (El decreases as the flow rate or shear rate is incremented). To compute the elasticity number appropriately for a given flow rate, throughout the remainder of the article we also use a shear-rate-dependent elasticity number ($\mathrm{El}(\dot{\gamma}) = \mathrm{Wi}/\mathrm{Re}(\dot{\gamma}) = 0.1\lambda\eta(\dot{\gamma})/\rho HD_h$), where the shear-rate-dependent Reynolds number is given by:

$$\mathrm{Re}(\dot{\gamma}) = \rho UD_h/\eta(\dot{\gamma}). \tag{1}$$

The shear-rate-dependent viscosity $\eta(\dot{\gamma})$ is evaluated from fits to the flow curves shown in Fig. 2(a, b). The viscosity data is fitted with the Carreau-Yasuda model (shown by the solid lines on the figure):

$$\eta(\dot{\gamma}) = \eta_\infty + (\eta_0 - \eta_\infty)\left[1 + (\dot{\gamma}/\dot{\gamma}^*)^a\right]^{(n-1)/a}, \tag{2}$$

where η_∞ is the infinite-shear-rate viscosity, η_0 is the zero-shear-rate viscosity, $\dot{\gamma}^*$ is the characteristic shear rate for the onset of shear-thinning, *n* is the "power-law exponent" in the shear-thinning region and *a* is a dimensionless fitting parameter that influences the sharpness of the transition from a constant shear viscosity to the power-law region. We note that this generalized Newtonian fluid (GNF) model accurately describes shear-thinning behavior, but does not account for fluid viscoelasticity, therefore its applicability is restricted. However, it has been shown that this simple model can be used to numerically predict the fully-developed velocity profiles in shear-thinning and viscoelastic fluids.[35] Within the OSCER device, assuming an ideal planar extensional flow, $\boldsymbol{v} = [\dot{\varepsilon}x, -\dot{\varepsilon}y, 0]$, the shear viscosity and hence the Reynolds number are evaluated at a characteristic shear rate given by $\dot{\gamma} = \sqrt{\frac{1}{2}\mathrm{II}_{\dot{\boldsymbol{\gamma}}}} = 2\dot{\varepsilon}$, where $\mathrm{II}_{\dot{\boldsymbol{\gamma}}}$ is the second invariant of the shear rate tensor $\dot{\boldsymbol{\gamma}} = \nabla\mathbf{v} + \nabla\mathbf{v}^{\mathbf{T}}$.

TABLE I. Details of the various polymer-solvent systems used in the study.

Polymer sample	Solvent	c [wt %]	c/c^*	L^2	η_s [mPa s]	η_0 [mPa s]	β	$El_{0.5}$	λ [ms]
PEO2	water	0.3	3	3360	1.0	3.8	0.26	0.039	4 ± 1
PEO2	46% glycerol	0.3	2	4430	4.3	30	0.14	1.7	26 ± 3
PEO2	66% glycerol	0.3	1.5	5380	13	86	0.15	14	75 ± 3
HA1.6	PBS	0.1	9	77	1.0	7.8	0.13	0.11	7 ± 1
HA2.6	PBS	0.1	13	112	1.0	21	0.047	0.56	15 ± 2
HA1.6	PBS	0.3	27	77	1.0	82	0.012	2.4	17 ± 3
HA2.6	PBS	0.3	39	112	1.0	853	0.0012	62	79 ± 10
PEO1*	66% glycerol	0.05	0.2	2580	13	14	0.93	0.18	6.5 ± 1

* The PEO1 sample is an $M_w = 1 \times 10^6$ g mol^{-1} PEO used by Haward *et al.*[8]

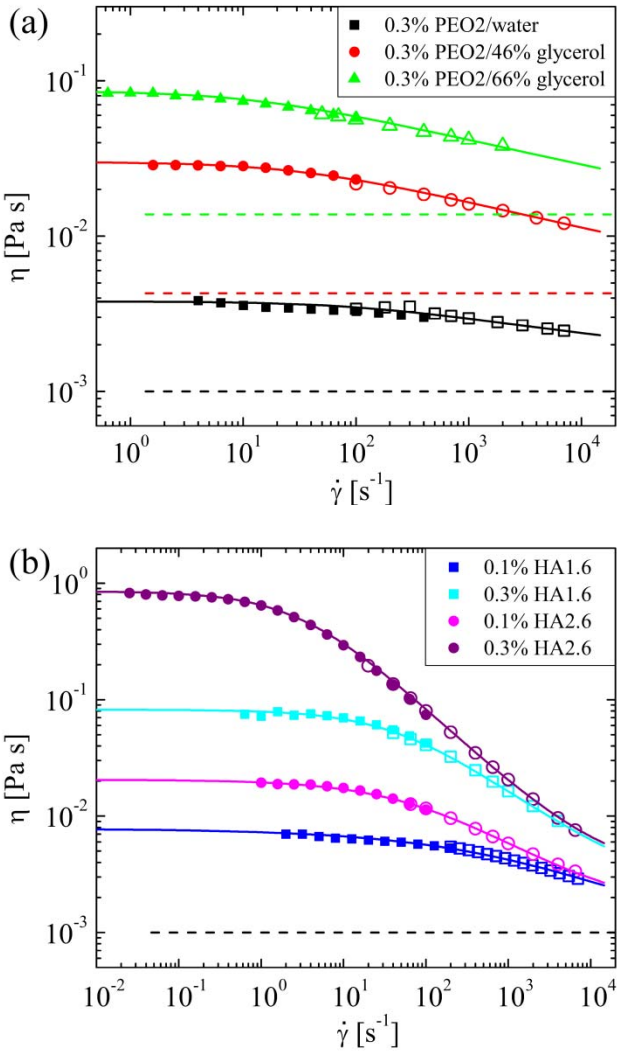

FIG. 2. Steady shear rheology of the various polymer solutions used in this study. (a) 0.3 wt % PEO2 in various aqueous glycerol mixtures, where the horizontal dashed lines indicate the viscosities of the respective solvents. (b) Hyaluronic acid solutions of various molecular weight and concentration dissolved in a phosphate buffered saline (PBS). The horizontal dashed line represents the viscosity of the PBS buffer solution. In both (a) and (b) the solid symbols represent data obtained using an AR-G2 stress-controlled rotational rheometer with a 40 mm diameter 2° cone-and-plate fixture. The hollow symbols are data obtained using an m-VROC microfluidic viscosimeter. The solid lines represent fits to the data using the Carreau-Yasuda model (Eq. 2).

B. Methods

The numerical optimization, design, fabrication and experimental operation of the OSCER device has been described in detail in a number of recent publications[8-10,16] and will not be repeated here. To visualize flow instabilities in the device, we use fast polarizing electro-optical modulation techniques to image the full-field flow-induced birefringence (FIB), which arises as polymer molecules unravel in the planar extensional flow field and the polymer solutions become optically anisotropic in local regions of high polymer orientation. Two birefringence imaging techniques are employed to measure FIB in the polymeric test solutions, and these are described below.

1. Liquid crystal compensator FIB imaging system

Initially an ABRIO polarizing microscope (CRI Inc., Woburn, MA) is used to measure the FIB in the polymer solutions as the nominal applied strain rate in the OSCER device is increased up until the onset of flow instability at some critical point denoted $(\mathrm{Re}_{crit}, \mathrm{Wi}_{crit})$ in Wi-Re space. The ABRIO system passes collimated and circularly polarized monochromatic light (wavelength 546 nm) first through the sample, then through a liquid crystal compensator and finally onto a CCD array. In the process of image acquisition, the CCD camera captures five individual frames with the liquid crystal compensator configured in a specific polarization state for each frame. Data processing algorithms described by Shribak and Oldenbourg[52] combine the five individual frames into a single full-field map of the optical retardation, $R(x,y)$, which quantifies the difference between the two orthogonal optical path lengths through the birefringent material. Assuming two-dimensional flow in the OSCER device, the retardation is related to the birefringence $\Delta n(x,y)$ by $R = d\Delta n$. The ABRIO system has a spatial resolution of approximately 2 μm/pixel (with a 4× objective lens), and provides a quantitative measure of the retardation to a nominal resolution of 0.02 nm, independent of the orientation angle of the sample. While the ABRIO system in its current form is thus excellent for measuring low levels of FIB in steady flows of complex fluids, the sequential 5-frame acquisition and data processing algorithm is slow and video capture is not possible; the acquisition rate is at present limited to approximately one frame every four seconds. Therefore the ABRIO is not suitable for visualizing the birefringence

fields in rapidly fluctuating time-dependent flows. In order to do this, a simpler but higher frame rate system is employed, as described below.

2. Crossed polarizer FIB imaging system

To achieve superior time resolution for characterizing the flow-induced birefringence following the onset of unsteady flow instabilities, we use a simple system consisting of a polarizer and an analyzer placed on either side of the OSCER device and crossed at ±45° to the direction of flow. Unlike the ABRIO microscope, this system is sensitive to the sample orientation, however this is relatively unimportant in the present experiment since polymer stretching in the OSCER is predominantly along the outflow direction (y = 0 axis) only, as previous experiments have clearly demonstrated.[8,10,16] The light source is a stabilized 660 nm, 60 mW fibre-coupled diode laser (Oz Optics Ltd., Ottawa, ON). Microscope objective lenses are used to expand the circular Gaussian laser beam in order to illuminate the largest possible region in the center of the OSCER geometry, while avoiding excessive scattering from the channel walls. To achieve the maximum possible signal-to-noise ratio, a quarter-wave plate is inserted into the optical line and the "linear detection method" described by Riddiford and Jerrard[53] is employed. A final microscope objective lens focuses light from the midplane of the OSCER device onto a deeply cooled $(-80^{o}\mathrm{C})$, very low noise, high quantum efficiency $(\approx 60\%)$, 14 bit, one-mega-pixel CCD array (Andor Technology PLC, Belfast, UK). The high sensitivity of the optical system means that birefringence signals can be detected with image exposure times as low as 2 to 5 ms, depending on the magnitude of the intrinsic birefringence of the polymer, the polymer concentration of the particular test fluid and the applied extension rate. Using 2 × 2 pixel binning, and a letter-box shaped region of interest around the outflow direction, image capture rates in excess of 100 frames per second (fps) can be achieved.

For each video captured with a particular flowing polymer solution, a single background image is also captured with the same acquisition settings, but with no fluid flowing through the OSCER device. Subsequent processing of the captured videos is performed using Image Pro Plus (MediaCybernetics Inc., Rockville, MD) and consists of first subtracting the background image and subsequently ratioing each pixel by the corresponding pixel in the background image (to

correct for the Gaussian laser beam intensity profile). The system is calibrated by using a de Sénarmont compensator to introduce known values of retardation into the optical line.

III. RESULTS

A. PEO2 aqueous solutions

We first use the ABRIO polarizing microscope system to image the steady birefringence fields in the OSCER device for the flow of the PEO2 solutions over a range of nominal imposed extension rates. For the PEO2 solution in 66 wt % glycerol ($El_{0.5} = 14$) at volume flow rates $Q < 2.8$ mL min^{-1} (equivalent to $\dot{\varepsilon} = 59.2$ s^{-1}, Re_{crit} = 0.4, Wi_{crit} = 4.4, El_{crit} = 10.9) the flow remains steady and symmetric. As shown by Fig. 3(a) for $Q = 1.6$ mL min^{-1}, a narrow birefringent strand is observed along the outflowing symmetry plane of the OSCER device ($y = 0$ axis), as previous experiments have also shown.[8,10,16] The birefringent strand indicates the localized stretching of polymer molecules only along streamlines that pass very close to the stagnation point where the residence times are high and hence large macromolecular strains can accumulate. The spatially-uniform intensity of the birefringent strand along the $y = 0$ axis is a result of the homogeneous extensional flow field in the OSCER device, which imposes a uniform strain rate on fluid elements as they flow downstream from the stagnation point. As the volume flow rate is increased above $Q = 2.8$ mL min^{-1}, the symmetric two-dimensional flow field becomes unstable and the birefringent strand becomes distorted and anti-symmetrical about the stagnation point, as shown by Fig. 3(b) for $Q = 3$ mL min^{-1} ($\dot{\varepsilon} = 63.5$ s^{-1}, Re = 0.44, Wi = 4.8, El = 10.8). Following the onset of this instability, the flow remains steady in time and the asymmetry can develop in either sense about the stagnation point, depending on random perturbations to the flow field. Since the Reynolds number is much lower than the Weissenberg number, we consider this flow instability to be analogous to the purely elastic flow bifurcation that was observed experimentally by Arratia *et al.*[30] and was modeled numerically by Poole *et al.*[32] in a conventional cross-slot geometry.

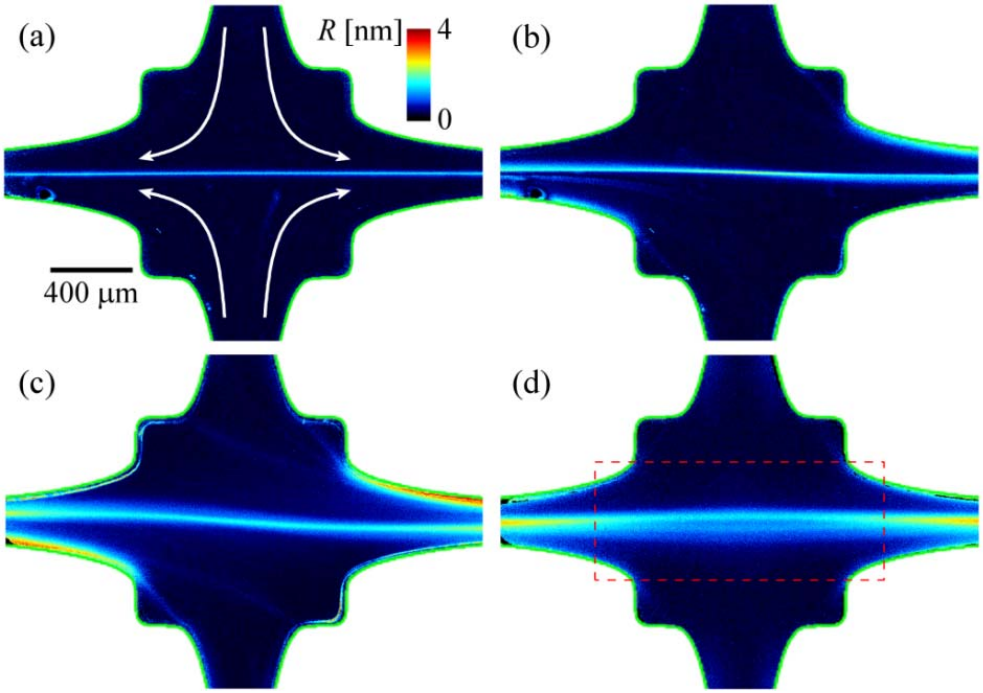

FIG. 3. Full-field false-color retardation images illustrating flow instabilities in the OSCER device for 0.3 wt % solutions of PEO2 in a variety of solvents. (a) Steady symmetric flow of the PEO2 solution in 66 wt % glycerol ($El_{0.5} = 14$, β = 0.15). The volume flow rate is $Q = 1.6$ mL min^{-1}, corresponding to a strain rate of $\dot{\varepsilon} = 33.8$ s^{-1} (Reynolds number Re = 0.22, Weissenberg number Wi = 2.54 and elasticity number El = 11). The white arrows indicate the flow direction. (b) A purely-elastic flow asymmetry observed for the PEO2 solution in 66 wt % glycerol at $Q = 3$ mL min^{-1}, $\dot{\varepsilon} = 63.5$ s^{-1}, Re = 0.44, Wi = 4.8, El = 10.8. (c) An elasticity-dominated flow asymmetry observed for PEO2 in 46 wt % glycerol ($El_{0.5} = 1.7$, β = 0.14) at $Q = 12$ mL min^{-1}, $\dot{\varepsilon} = 254$ s^{-1}, Re = 5.4, Wi = 6.6, El = 1.2. (d) An inertio-elastic instability for a PEO2 solution in pure water ($El_{0.5} = 0.039$, β = 0.26) at a flow rate of $Q = 26$ mL min^{-1}, $\dot{\varepsilon} = 550$ s^{-1}, Re = 64, Wi = 2.2, El = 0.034. The area within the dashed red rectangle indicates the region of interest used for the high speed visualization of birefringence patterns presented in subsequent figures.

For the less viscous PEO2 solution in 46 wt % glycerol at $Q = 12$ mL min^{-1} (El = 1.2), we also observe a steady asymmetric birefringent strand above a critical flow rate $(Re_{crit,}\ Wi_{crit}) = (4.9, 6)$, as shown in Fig. 3(c). In this case the critical values of Re and Wi are

similar in magnitude (providing an elasticity number for this fluid only slightly greater than unity), we therefore consider this an "elasticity-dominated" instability.

For the PEO2 solution in pure water (the least viscous and least elastic of the three PEO2 solutions with $\mathrm{El}_{0.5} = 0.039$), a different mode of instability is encountered as the flow rate is increased. For volume flow rates $Q < 25$ mL min^{-1} (equivalent to $\dot{\varepsilon} = 529$ s^{-1}, $\mathrm{Re}_{crit} = 62$, $\mathrm{Wi}_{crit} = 2.1$, $\mathrm{El}_{crit} = 0.034$) the flow remains steady and symmetric and the birefringent strand appears qualitatively similar to the example shown in Fig. 3(a). However, for $Q > 25$ mL min^{-1} the flow becomes unsteady and time-dependent. As shown by Fig. 3(d), in the ABRIO microscope we observe that the birefringent strand maintains symmetry about the $x = 0$ axis, but becomes significantly broader and less intense in the central region of the OSCER device, compared with locations further downstream. Since in this case the Weissenberg number is $\mathrm{Wi} > 1$, but is significantly smaller in magnitude than the Reynolds number (i.e. El << 1) we refer to this as an inertio-elastic instability. It is worth emphasizing that planar stagnation point flows of Newtonian fluids in the OSCER device remain stable up to Reynolds numbers $\mathrm{Re} \approx 30$, so in this case the moderate elasticity of the fluid appears to play a stabilizing role on the onset of the inertial instability. In the time-averaged image presented in Fig. 3(d), intensity striations are clearly visible in the vicinity of the stagnation point, conveying the impression that the birefringent strand of stretched polymer may actually be fluctuating in position during the process of image acquisition. To gain additional insight into the nature of this time-dependent inertio-elastic flow instability, we now examine the fluid dynamics of this PEO2 solution in more detail using the high-frame rate birefringence imaging set-up described in Section IIB2.

In Fig. 4(a, b) we present examples of steady symmetric flow of the PEO2 solution in pure water ($\mathrm{El}_{0.5} = 0.039$) at two different flow rates (Q = 10 and 20 mL min^{-1}), both captured with an exposure time of 3 ms. Movies captured at around 100 fps are also available to demonstrate the stability of the birefringent strands (and hence the flow field) at these flow rates. The dashed red box superimposed on Fig. 3(d) indicates the letter-box region of interest that was selected in order to achieve this high-frame rate imaging. As shown by Fig. 4(a, b), increasing the flow rate from 10 to 20 mL min^{-1} (or equivalently incrementing the Weissenberg number from Wi = 0.85 to Wi = 1.7) results in an increase in the width of the birefringent strand and a significant increase in its peak intensity along the outflow axis ($y = 0$).

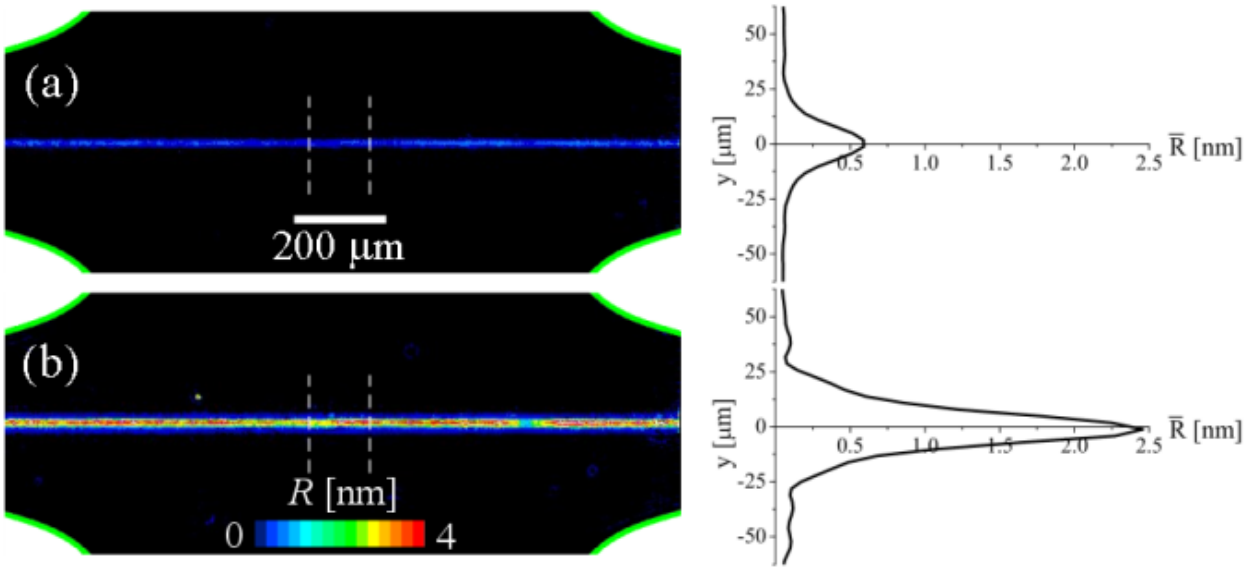

FIG. 4. Examples of steady birefringent strands in the OSCER for flow of the 0.3 wt % solution of PEO2 in water ($\mathrm{El}_{0.5} = 0.039$, β = 0.26). (a) Q = 10 mL min^{-1}, $\dot{\varepsilon} = 212$ s^{-1}, Re = 23, Wi = 0.85, El = 0.37. (b) Q = 20 mL min^{-1}, $\dot{\varepsilon} = 424$ s^{-1}, Re = 48.4, Wi = 1.7, El = 0.35. Images were captured with an exposure time of 3 ms (videos at 100 fps) and the same color contour scheme is used. To the right of each image are one-dimensional retardation profiles across the birefringent strands, averaged along the x-direction between the vertical dashed lines $-75\ \mu\mathrm{m} \le x \le 75\ \mu\mathrm{m}$. Enhanced online.

Upon further increasing the flow rate to Q = 25 mL min^{-1} (Re_{crit} = 62, $\mathrm{Wi}_{crit} = 2.1$, see Fig. 5) the birefringent strand begins to manifest the flow instability previously documented with the ABRIO system in Fig. 3(d). The images in Fig. 5(a, b) both correspond to the same flow rate but are captured approximately 0.7 s apart, and they show that both the width and intensity of the birefringent strand varies in time. A movie of this phenomenon captured at around 100 fps is also available. Frame-by-frame analysis of retardation profiles taken across the width of the birefringent strands and averaged along the x-direction between the dashed white lines shown in Fig. 5(a, b) (corresponding to $-75\ \mu\mathrm{m} \le x \le 75\ \mu\mathrm{m}$ or $\Delta x = 150\ \mu\mathrm{m}$) can be used to create a space-time diagram depicting the variation of optical retardation in the strand with time $\bar{R}(y,t) = \frac{1}{\Delta x}\int_{-\Delta x/2}^{\Delta x/2} R(x,y,t)dx$ in the locality of the stagnation point, as shown in Fig. 5(c). This clearly shows that the variation in width of the birefringent strand is oscillatory with a period

$T \approx 1.4$ s. Qualitatively, this instability seems to be similar to the experimental observations reported by Müller *et al.*[41] for nearly monodisperse polystyrene solutions in an axisymmetric opposed jets apparatus and to the computations reported by Xi and Graham[34] using a FENE dumbbell model.

According to Xi and Graham[34] the long period (relative to the relaxation time, λ) arises from couplings between the progressive perturbation of the flow field and the finite time over which macromolecules accumulate strain. In their simulations with FENE dumbbells, Xi and Graham[34] report $T/\lambda \approx 14$, whereas in our experiment the period of oscillation is considerably longer than this ($T/\lambda \approx 250$). Müller *et al.*[41] were not able to measure a period for the instability they observed, but state that the oscillations were "rapid". We note here that the simulations of Xi and Graham[34] were performed under inertialess conditions (Re = 0), whereas our instability arises for $\mathrm{Re}_{crit} = 62$. Also, the simulations were carried out for dilute dumbbell concentrations such that the viscosity ratio was $\eta_s/\eta_0 \equiv \beta = 0.95$ (higher concentrations, or lower β could not be simulated due to the occurrence of numerical instabilities). For our semi-dilute test fluid the viscosity ratio is much lower ($\beta = 0.26$) than the value used in simulations and shear-thinning may also complicate the analysis. It is also possible that the long period we observe is due to the polydispersity of the PEO2 sample (typically $M_w/M_n \approx 7$ for a commercially available sample such as that used here). The corresponding spread of molecular relaxation times in the sample could be expected to broaden the characteristic period of this oscillatory instability. In future work we intend to investigate the effect of polydispersity on the instability more fully.

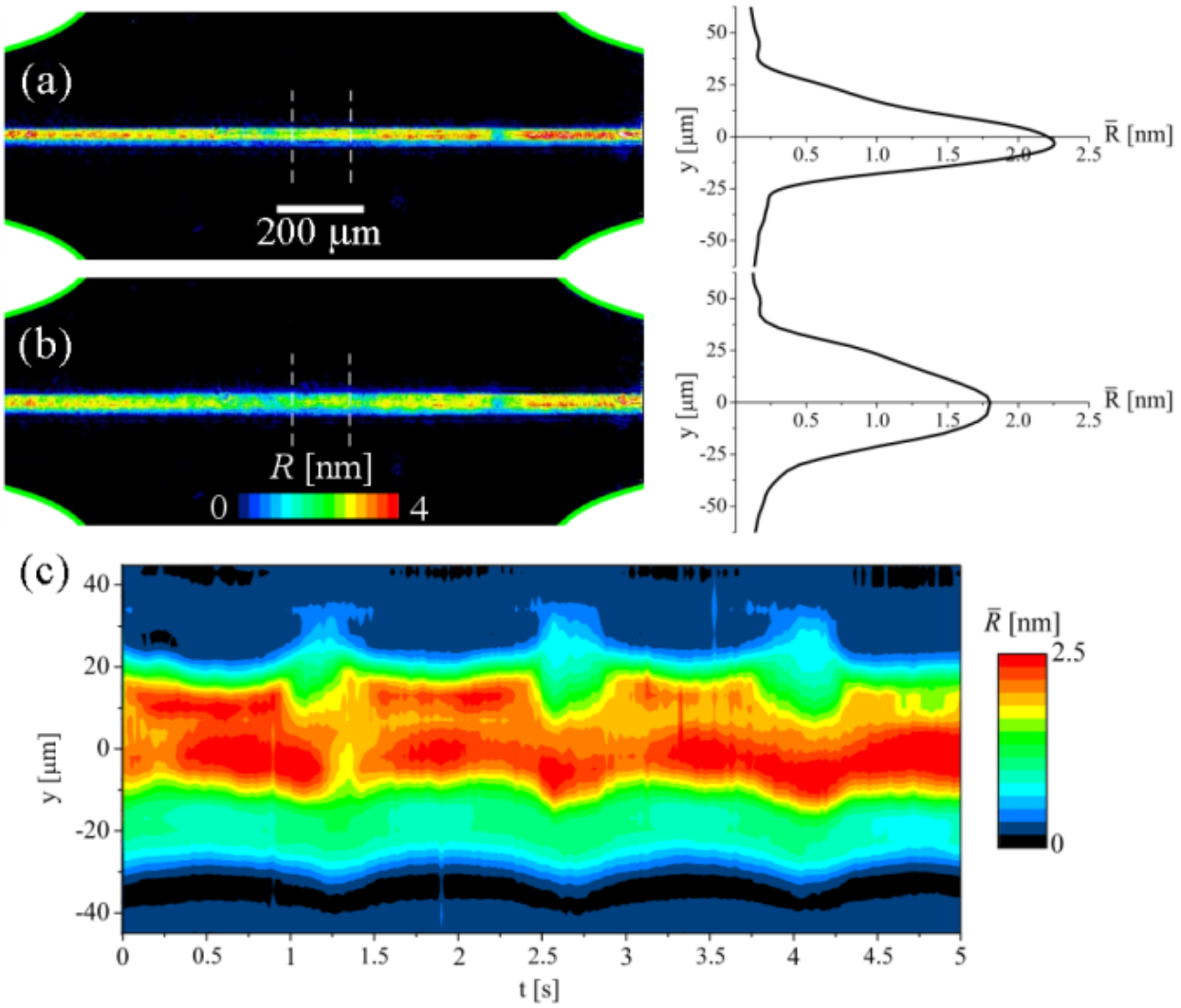

FIG. 5. Still images of a birefringent strand in the OSCER for flow of the PEO2 solution in water ($\mathrm{El}_{0.5} = 0.039$, $\beta = 0.26$) at $Q = 25$ mL min^{-1}, $\dot{\varepsilon} = 529$ s^{-1}, Re = 62, Wi = 2.1, El = 0.034. (a) The strand as it appears at an arbitrary time has a cross-sectional profile like that shown to the right, where the optical intensity is averaged between $-75\ \mu\mathrm{m} \le x \le 75\ \mu\mathrm{m}$, as marked by the vertical dashed lines. (b) The strand as it appears approximately 0.7 s after (a). As shown by the retardation profile to the right the strand width has increased substantially and the intensity has reduced. (c) As shown in this space-time diagram, the broadening/narrowing of the birefringent strand is cyclic with a period of around 1.4 s. Enhanced online.

When the flow rate is increased only slightly further to $Q = 26$ mL min^{-1} (Wi = 2.2) the oscillatory instability develops in a dramatic fashion. Two distinct modes of instability can be

observed, as shown in Fig. 6(a, b). Most commonly, still images appear to show two birefringent strands widely separated near $x = 0$ and converging downstream of the stagnation point. This seems on first sight to be analogous to the birefringent pipe structures reported in axisymmetric opposed jet flows of polymer solutions,[41,43] however video imaging (in this instance captured at approximately 80 fps, with 5 ms exposure) shows clearly that the strands are not steady in space or time but fluctuate rapidly. A space-time diagram derived from analysis of the retardation intensity measured between the dashed white lines in Fig. 6(a) is presented in Fig. 6(c), clearly showing this spatio-temporal fluctuation. A second mode of instability, less often observed, is illustrated in Fig. 6(b). In this case the appearance is of two birefringent strands crossing near the stagnation point. There are only two plausible explanations for this behavior: 1) the flow has become three-dimensional and there are indeed two birefringent strands with opposite symmetry separated in the z-direction and crossing near the stagnation point, or 2) there is one birefringent strand oscillating in an antisymmetric mode. We believe that the latter is the most likely explanation, and note that taken together, Fig. 6(a, b) appear analogous to the first two harmonics of a taut vibrating string or sheet, with Fig. 6(a) corresponding to the first harmonic ($n = 1$) and Fig. 6(b) corresponding to the second harmonic ($n = 2$).

As we illustrate in Fig. 7, an additional small increase in the flow rate up to $Q = 27$ mL min^{-1} ($Re = 67.1$, $Wi = 2.3$) results in another flow transition that leads to large amplitude, apparently chaotic, motions of the birefringent strand for the PEO2 solution in the purely aqueous solvent.

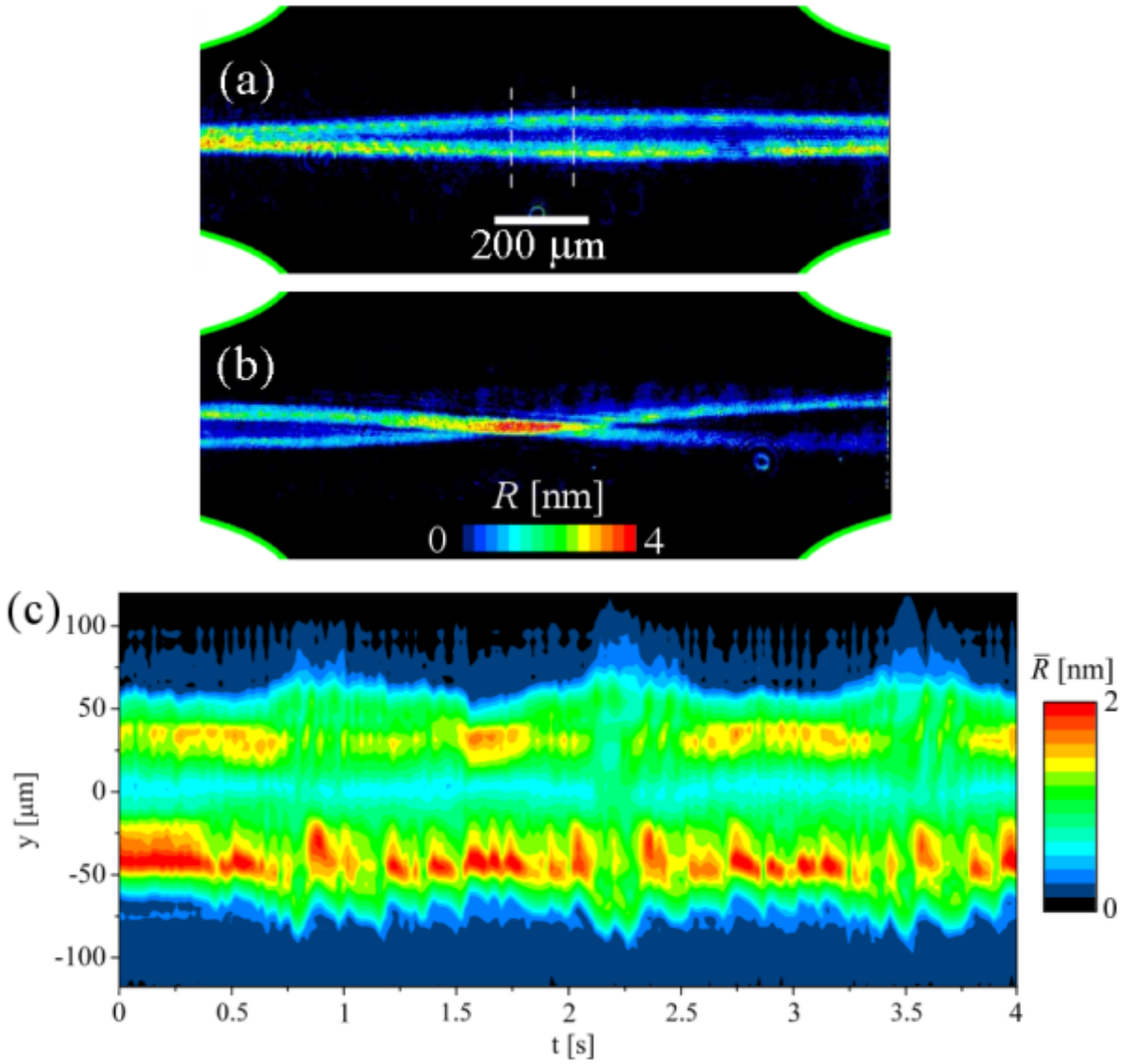

FIG. 6. Images of birefringent strands in the OSCER for flow of the PEO2/water solution ($El_{0.5} = 0.039$, $\beta = 0.26$) at $Q = 26$ mL min^{-1}, $\dot{\varepsilon} = 550$ s^{-1}, Re = 64.4, Wi = 2.2, El = 0.034. In (a) the strand appears to have bifurcated into two separate strands with maximum separation near the stagnation point. In (b), which was only observed on rare occasions, two birefringent strands appear to cross near the stagnation point. In both cases (a) and (b), the strands are unsteady and show strong spatio-temporal fluctuations. Images were captured with an exposure time of 5 ms (video rate 80 fps). (c) A space-time diagram corresponding to the movie from which Fig. 6(a) is taken. The average optical retardation $\bar{R}(y,t)$ in each frame is averaged in the outflow direction between the dashed white lines located at $-75\ \mu\text{m} \le x \le 75\ \mu\text{m}$ shown in Fig 6(a). Enhanced online.

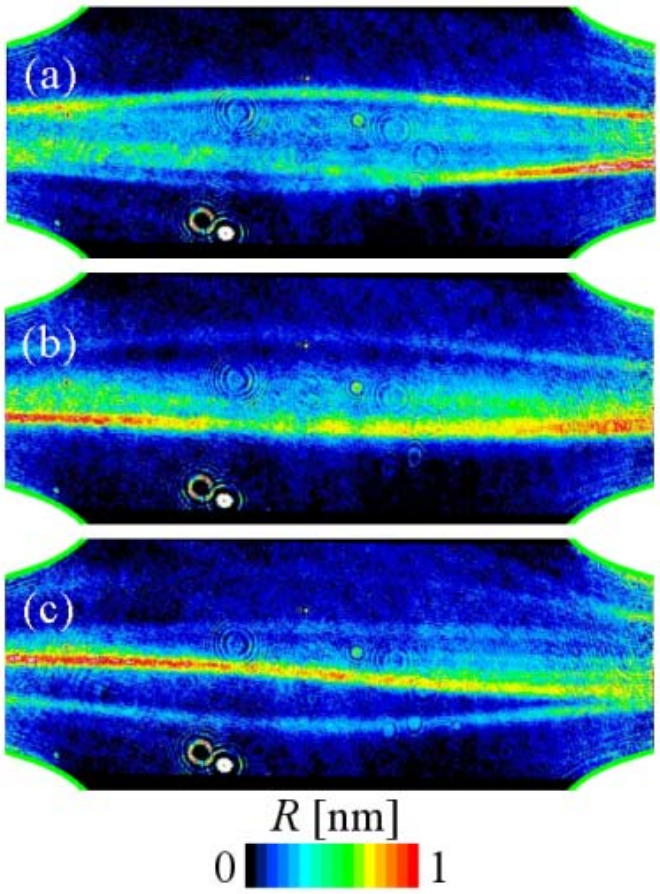

FIG. 7. Still images of birefringent strands imaged in the OSCER for flow of the PEO2/water solution ($El_{0.5} = 0.039$, β = 0.26) at Q = 27 mL min^{-1}, $\dot{\varepsilon} = 571\ s^{-1}$, Re = 67.1, Wi = 2.3, El = 0.034. Multiple strand positions are observed during each exposure. Images (a), (b) and (c) were captured with an exposure time of 3 ms (video rate of 100 fps) and over a total time period of $\Delta t \approx$ 100 ms. Enhanced online.

The results of Figs. 4 – 7 can be combined with data obtained at intermediate Weissenberg numbers and summarized in the form of a bifurcation diagram in the y-Wi plane, as shown in Fig. 8(a). This image is formed by extracting the retardation profiles $\bar{R}(y)$ averaged between $-75\ \mu m \le x \le 75\ \mu m$ (see the domain indicated by the white box in Fig. 8(b)) and assembling them into a contour plot as a function of the Weissenberg number. A similar approach was taken by Carrington *et al.*[43] for presenting the FIB structures they observed over a range of Wi in the opposed jets apparatus. In Fig. 8(a) we observe that for 0.4 < Wi < 2 the birefringent strand grows steadily and monotonically in width and intensity. Above Wi = 2 the inertio-elastic

instability begins to develop rapidly and at $\mathrm{Wi} = 2.1$ the temporally-averaged retardation data shows two spatially-separated birefringent strands of lower intensity (as discussed above). For comparison, in Fig. 8(c) we also show a similar plot derived from retardation profiles obtained with the PEO2 solution in 46 wt % glycerol. In this case the birefringent strand remains stable and symmetric about the center plane up to a much higher $\mathrm{Wi}_{crit} = 6$, before developing an elastically-dominated flow asymmetry (as shown in Fig. 3(c)).

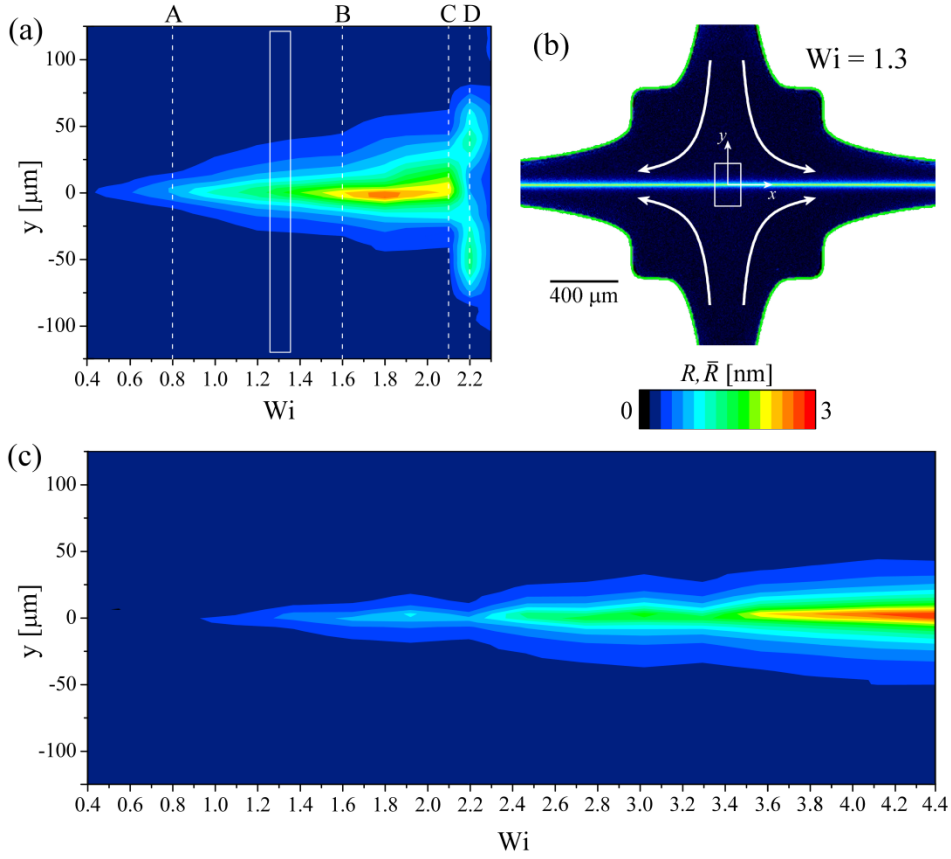

FIG. 8. (a) Experimental bifurcation diagram in the y-Wi plane depicting the evolution of the intensity of the birefringent strand with Weissenberg number for the PEO2 solution in water ($\mathrm{El}_{0.5} = 0.039$, $\beta = 0.26$). The optical retardation of the strand intensifies and broadens with Wi until the onset of the inertio-elastic instability at $\mathrm{Wi} \approx 2$. The locations marked by vertical dashed lines and capital letters correspond to previously presented figures: A) Fig. 4(a); B) Fig. 4(b); C) Fig. 5; D) Fig. 6(a). The data contained within the white rectangle centered on Wi = 1.3 is obtained from the area within the white box indicated in part (b), shown alongside. (c) Space-Wi diagram depicting the evolution of the birefringent strand with Weissenberg number for a more viscous PEO2 solution in 46% glycerol ($\mathrm{El}_{0.5} = 1.7$, $\beta = 0.14$).

B. HA aqueous solutions

The behavior of the hyaluronic acid (HA) solutions dissolved in phosphate buffered saline (PBS) follow similar qualitative trends to the PEO2 solutions described above. Over a range of flow rates up to moderate Wi and Re, the flow field remains stable and a steady, uniform and symmetric birefringent strand is observed, aligned along the outflowing symmetry axis of the OSCER geometry. However, above critical values $(\mathrm{Re}_{crit}, \mathrm{Wi}_{crit})$, flow instabilities are manifested by distortions of the birefringent strands that can be unambiguously classified as either purely elastic asymmetries or inertio-elastic instabilities.

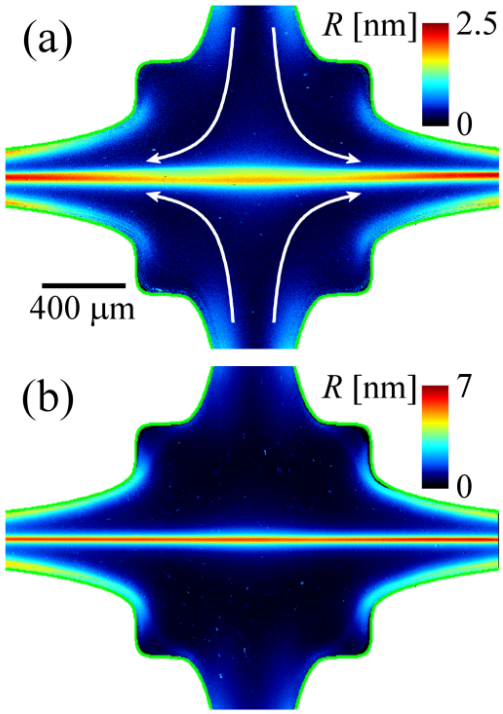

FIG. 9. Full-field false-color retardation images illustrating onset of flow instabilities in the planar stagnation point flow of hyaluronic acid (HA) based polymer solutions. (a) Inertio-elastic instability in a 0.1 wt% solution of HA1.6 in PBS ($\mathrm{El}_{0.5} = 0.11$, β = 0.13) at a flow rate $Q = 18$ mL min^{-1}, $\dot{\varepsilon} = 381$ s^{-1}, Re = 29.5, Wi = 2.7, El = 0.09. (b) Weak inertio-elastic flow instability (as observed close to the critical onset conditions) in a 0.1 wt% solution of HA2.6 in PBS ($\mathrm{El}_{0.5} = 0.56$, β = 0.047). The flow rate is $Q = 20$ mL min^{-1}, $\dot{\varepsilon} = 423$ s^{-1}, Re = 23.3, Wi = 6.3, El = 0.27.

In Fig. 9 we present images obtained using the ABRIO polarizing microscope system showing the instabilities that are observed in 0.1 wt % HA/PBS solutions. In the less elastic 0.1 wt % HA1.6 solution ($El_{0.5}$ = 0.11, Fig. 9(a)), a clear inertio-elastic instability is encountered for flow at rates above $Q = 12$ mL min^{-1}, Re_{crit} = 19, Wi_{crit} = 1.8. In the higher molecular weight and more viscoelastic 0.1 wt % HA2.6 solution ($El_{0.5}$ = 0.56), the flow remains stable to significantly higher Wi_{crit} = 5.7 (corresponding to a similar critical Reynolds number Re_{crit} = 20), beyond which we observe a weak inertio-elastic instability characterized by a small increase in the width of the birefringent strand near to the stagnation point, see Fig. 9(b)).

We re-emphasize here that until the onset of flow instabilities the OSCER device can be effectively used as a planar extensional rheometer for complex fluids.[8,10,16] One way to calculate the local extensional viscosity is to make measurements of the birefringence (Δn) as a function of the imposed strain rate ($\dot{\varepsilon}$), as illustrated in Fig. 10. For the case of HA/PBS solutions, the stress-optical coefficient has recently been measured experimentally to be $C = 1.82\times10^{-8}$ Pa^{-1},[50] enabling a direct conversion from birefringence into a principal stress difference ($\Delta\tau$) using the stress-optical rule.[56] The extensional viscosity of these mobile polymer solutions at high deformation rates can thus be determined as a function of the strain rate from the definition $\eta_E(\dot{\varepsilon}) = \Delta\tau/\dot{\varepsilon}$. We estimate maximum values for the extensional viscosity prior to the onset of unstable flow (at a strain rate of $\dot{\varepsilon} \approx 250$ s^{-1}) of $\eta_{E,\max} \approx 0.2$ Pa s and $\eta_{E,\max} \approx 0.6$ Pa s for the 0.1 wt % HA1.6 and HA2.6 solutions, respectively. Compared with the shear viscosities of the fluids, $\eta(\dot{\gamma})$, evaluated at a shear rate of $\dot{\gamma} = 2\dot{\varepsilon} = 500$ s^{-1}, we obtain corresponding Trouton ratios of $Tr = \eta_E/\eta \approx$ 43 and 82.

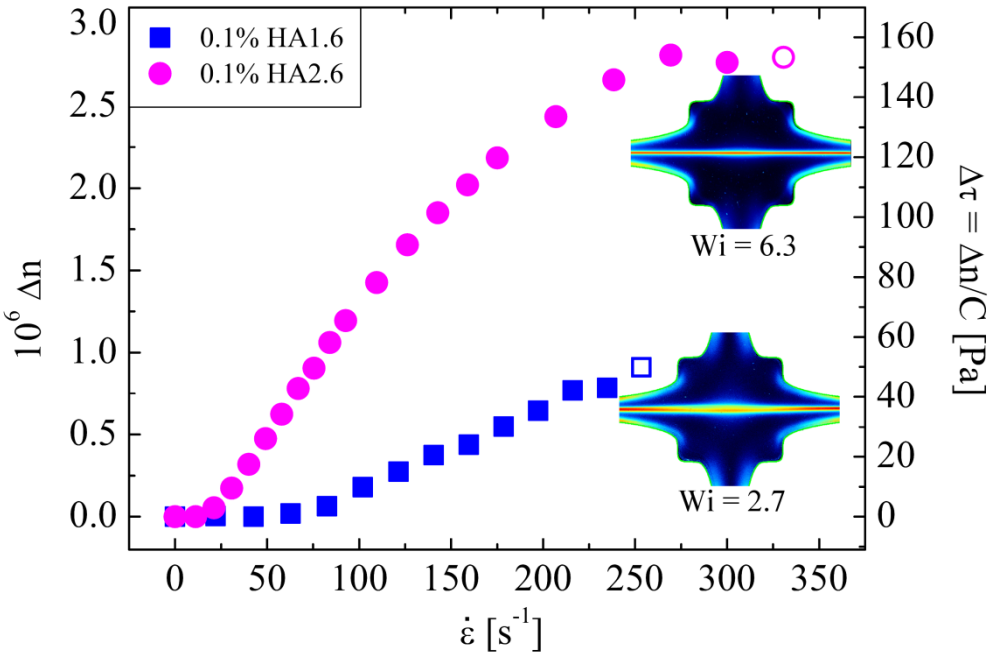

FIG. 10. Evolution of birefringence and stress as a function of the imposed strain rate in the OSCER for 0.1 wt % HA solutions. The open symbols represent the last measurements made before the onset of instability. Up until the onset of flow instabilities the device can be used as a planar extensional rheometer for complex fluids.

Of course, this method of determining the extensional viscosity involves the implicit assumption that the stress-optical rule remains valid as macromolecules become significantly deformed from their equilibrium Gaussian coiled state. This assumption clearly must break down at some point during polymer stretching, and this becomes most apparent as polymer chains approach their finite extensibility limit; here the birefringence must necessarily saturate although the stress can continue to increase with increasing strain rate. However, it has been shown using combined pressure drop and birefringence measurements for various fluids in stagnation point flow experiments that stress and birefringence can vary co-linearly over a surprisingly wide range of extension rates, such that a single-valued stress-optical coefficient can often be used in order to estimate $\eta_E(\dot{\varepsilon})$, as described above.[8,36,54]

As the concentration of HA in the solutions is increased to 0.3 wt %, the fluids become increasingly viscoelastic. The relaxation time (λ) and the polymer contribution to the viscosity ($\eta_p = \eta_0(c) - \eta_s$) both increase, resulting in a substantially increased elasticity number.

Nevertheless, at $\mathrm{El} \approx 0.6$ the 0.3 wt % HA1.6 solution still displays a clear inertio-elastic instability above $(\mathrm{Re}_{crit}, \mathrm{Wi}_{crit}) = (18,13)$, as illustrated in Fig. 11(a) for flow conditions of $Q = 50$ mL min^{-1}, (Re = 30.6, Wi = 18). On the other hand, for the HA2.6 solution, increasing the elasticity number to El >> 1 results in a pronounced transition from an inertio-elastic instability mode (Fig. 9(b)) to a purely elastic asymmetric mode of instability for flow at rates exceeding $(\mathrm{Re}_{crit}, \mathrm{Wi}_{crit}) = (0.17,3.5)$, as illustrated in Fig. 11(b). The higher concentration of polymer and the higher stress-optical coefficient for HA also result in more evident stress boundary layers near the curved walls of the OSCER device. Here the flow is no longer purely extensional in character; the local shear rate is high near the walls and both the shear stress and the first normal stress difference contribute to the principal stress difference and optical retardation exhibited by the fluid.

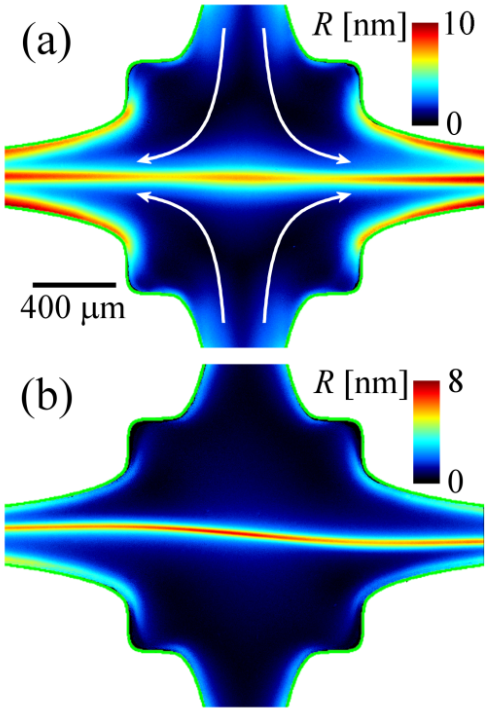

FIG. 11. (a) A strong varicose-like inertio-elastic instability in a more concentrated 0.3 wt% solution of HA1.6 ($\mathrm{El}_{0.5} = 2.4$, β = 0.012) at a flow rate of $Q = 50$ mL min^{-1}, $\dot{\varepsilon} = 1058$ s^{-1}, Re = 30.6, Wi = 18, El = 0.6. (b) A steady but asymmetric birefringent strand indicative of a purely elastic flow instability in a highly elastic 0.3 wt% solution of HA2.6 ($\mathrm{El}_{0.5} = 62$, $\beta = 0.0012$) at a flow rate of $Q = 3$ mL min^{-1}, $\dot{\varepsilon} = 63.5$ s^{-1}, Re = 0.3, Wi = 5, El = 16.7.

The oscillatory nature of the inertio-elastic flow instabilities in the HA-based polymer solutions is similar to that observed in the PEO2 solutions. An example is given for the 0.3 wt % HA1.6 in Fig. 12, using the high-speed birefringence imaging system. The flow conditions are the same as for Fig. 11(a), $Q = 50$ mL min^{-1}, with the exposure time set to 2 ms and the video acquisition rate set to 137 fps.

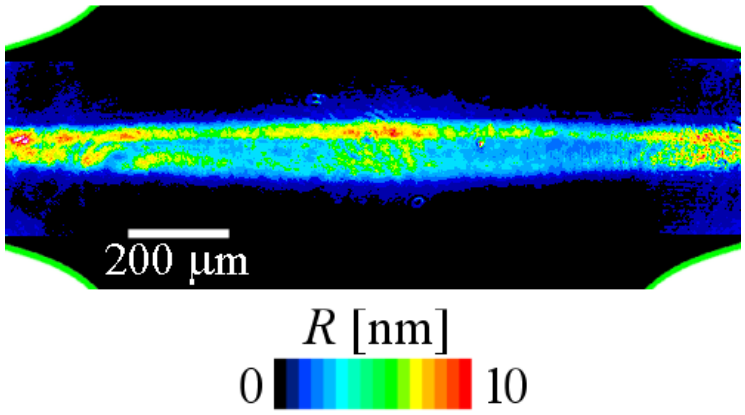

FIG. 12. Inertio-elastic instability in the 0.3 wt % solution of HA1.6 in PBS ($El_{0.5} = 2.4$, $\beta = 0.012$) at $Q = 50$ mL min^{-1}, $\dot{\varepsilon} = 1058$ s^{-1}, Re = 30.6, Wi = 18, El = 0.6 imaged using the high-speed birefringence method and an exposure time of 2 ms (video rate 137 fps). Enhanced online.

IV. DISCUSSION

In Table II we compile the critical conditions for the onset of flow instabilities in all of the various test fluids characterized in Table I. Along with Re_{crit}, Wi_{crit} and the corresponding elasticity number $El_{crit} = Wi_{crit}/Re_{crit}$ at the onset point of instability, we list the values of the other key rheological parameters we expect to play a role in influencing the onset point (i.e. c, β and L^2) and we also denote the mode of instability as either purely elastic or inertio-elastic.

Some general trends can be observed in Table II. For a given class of fluid (e.g. the PEO2 solutions) increasing the extensibility of the polymer chains L^2 tends to result in a greater likelihood of purely elastic instabilities developing at lower Wi_{crit}. Likewise, increasing the polymer concentration c (or, equivalently, decreasing β) also appears to drive the dominant

mode of instability towards the purely elastic steady asymmetric flow at lower Wi_{crit}. In this regard our experiments are in general agreement with the trends reported by Rocha *et al.*[33] who performed simulations varying the same parameters using a FENE dumbbell model in a standard-shaped cross-slot geometry. However, the most striking result in Table II is found in comparison between the value of El_{crit} and the corresponding instability mode. For a wide range of fluids of different molecular weights, concentrations, solvent viscosity, flexibility and steady shear rheology, we find that for $\mathrm{El}_{crit} < 1$ inertio-elastic instabilities are observed, whereas for $\mathrm{El}_{crit} > 1$ steady symmetry-breaking elastic instabilities dominate.

TABLE II. Critical limits of flow stability for the various polymeric test solutions.

Polymer sample	Solvent	c [wt.%]	β	L^2	Re_{crit}	Wi_{crit}	El_{crit}	Instability mode
PEO2	water	0.3	0.26	3360	62	2.1	0.034	inertio-elastic
PEO2	46% glycerol	0.3	0.14	4430	4.9	6	1.2	elastic
PEO2	66% glycerol	0.3	0.15	5380	0.4	4.4	11	elastic
HA1.6	PBS	0.1	0.13	77	19	1.8	0.095	inertio-elastic
HA2.6	PBS	0.1	0.047	112	20	5.7	0.29	inertio-elastic
HA1.6	PBS	0.3	0.012	77	18	13	0.72	inertio-elastic
HA2.6	PBS	0.3	0.0012	112	0.17	3.5	21	elastic
PEO1*	66% glycerol	0.05	0.93	2580	16	2.8	0.18	inertio-elastic

* The PEO1 sample corresponds to the $M_w = 1 \times 10^6$ g mol^{-1} PEO solution used by Haward *et al.*[8]

The trends observed with changes in c (or β) and L^2 are consistent with rheological expectations. Varying those parameters systematically changes the fluid viscosity (η) and the polymer relaxation time (λ), which are both incorporated in the magnitude of the elasticity number. The elasticity number is thus the primary governing parameter determining the dominant instability mode that is observed in viscoelastic fluid flows near planar stagnation points.

The elasticity number can be readily visualized as representing the trajectory through Wi-Re space for a set of experiments with a given viscoelastic fluid over a range of applied strain rates. Because the fluids are, in general, shear-thinning, the Reynolds number increases non-linearly with the deformation rate and therefore the elasticity number also depends upon the flow

rate through the OSCER device. The trajectories for the fluids studied here are presented in Fig. 13, where the axes are represented on logarithmic scales due to the very wide ranges of Re and Wi that are covered. On the trajectory for each fluid the onset point for instability $(\mathrm{Re}_{crit}, \mathrm{Wi}_{crit})$ is marked by an open circle in the case of elastic instability and a closed circle in the case of inertio-elastic instability.

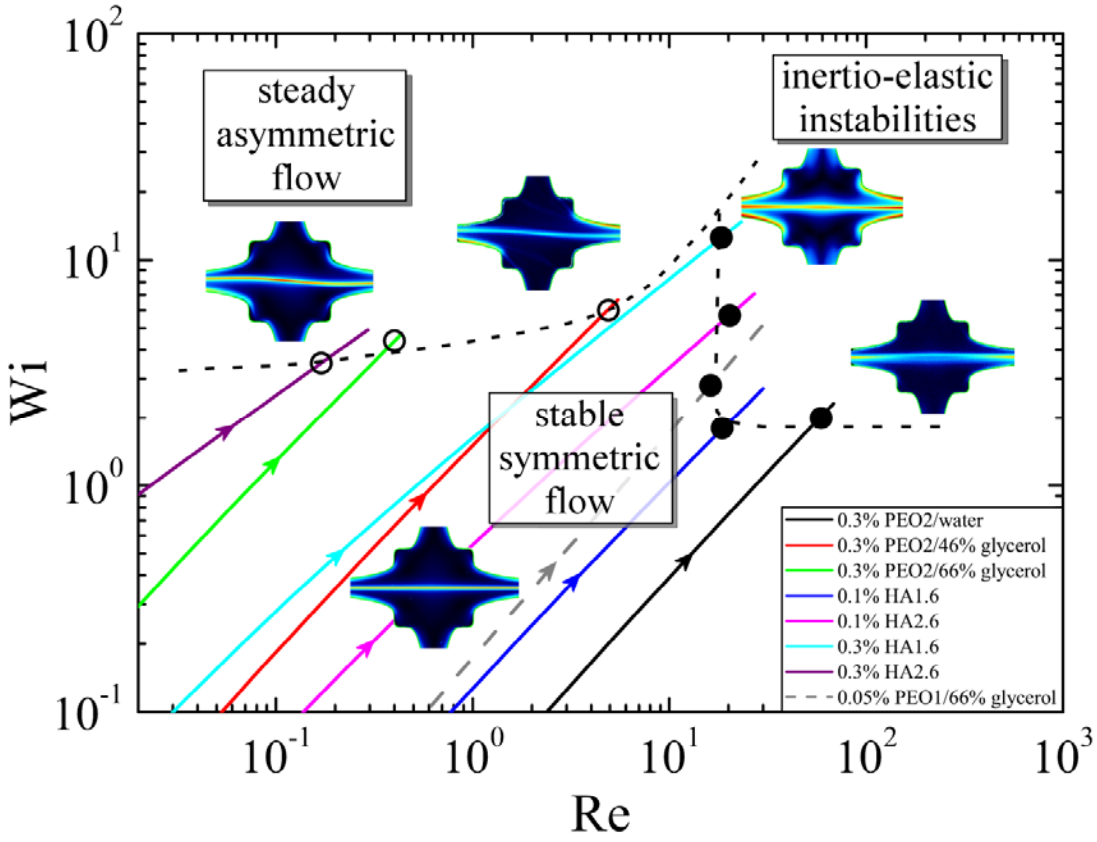

FIG. 13. Stability diagram for polymer solutions in planar stagnation point flow in the Reynolds number - Weissenberg number operating space. The dashed grey line indicates the trajectory through Wi-Re space for the PEO1 solution studied by Haward *et al.*[8] Shear-thinning results in gradual changes in the slope of these trajectories. The hollow symbols indicate the onset points of purely-elastic flow instabilities and the solid symbols indicate the onset of inertio-elastic flow instabilities.

The critical onset conditions for flow instabilities in Wi-Re operating space clearly demarcate the limits of operability of the OSCER device as a planar extensional rheometer. For

conditions such that $\mathrm{Wi} \geq 2$, $\mathrm{Re} \geq 10$ and $\mathrm{El} < 1$ (i.e. the upper-right quadrant of Fig. 13), the rheometric capabilities are limited by the onset of time-dependent inertio-elastic instabilities. For more elastic fluids (El > 1) inertial effects are less important, but at sufficiently high Weissenberg numbers (i.e. the upper-left section of Fig. 13), we expect the onset of a steady symmetry-breaking purely elastic instability to limit the utility of the device. This operability diagram has broad applicability to experiments using a wide range of polymer solutions with different rheological properties and molecular parameters. As more fluids are tested in the OSCER it will be interesting to see if their El trajectories and critical points for onset of instabilities are consistent with this operability diagram.

It will also be important to test fluids in OSCER devices of different length scales H and aspect ratios ($\alpha = d/2H$) to see whether this operating diagram is robust to variations in the flow geometry, which should already be properly accounted for in the definition of the elasticity number. This has been found not to be the case in similar studies exploring mixed flows of complex fluids in microfabricated entrance geometries,[23,24] where geometrical factors that are not accounted for in the definition of the elasticity number (such as the contraction ratio and downstream capillary length) have been shown to significantly affect the onset conditions for viscoelastic flow instabilities. [26-28]

As noted above in Section III. A, the appearance of the birefringent strand during the inertio-elastic instability in the OSCER device is highly reminiscent to the development of a standing elastic wave on a stretched string (see Fig. 6). However, if this is indeed the case, the frequency of the oscillation is too high for us to resolve unambiguously even with our improved high frame rate birefringence imaging method (which provides capture rates on the order of 100 fps). For image acquisition rates lower than the Nyquist frequency, the image results will be aliased, hence the birefringence intensity will be greatest at locations where the vibrating elastic strand spends the greatest time during its cycle, i.e. at the points of greatest amplitude and lowest velocity. Note that if Nyquist aliasing is important, the absolute magnitude of the retardation values shown in Fig. 6 is quite nominal since the residence time of the birefringent strand at any location in the image is uncertain and may be much less than the time over which the image is acquired.

If we consider the average centerline retardation $\overline{R} \approx 2.4$ nm just *before* the onset of instability (c.f. Fig. 4(b)), we can estimate the dimensionless birefringence to be

$\Delta n = R/d \approx 1.2\times10^{-6}$. Assuming validity of the stress-optical rule, which gives the principal stress difference as $\Delta\tau = \tau_{xx} - \tau_{yy} = \Delta n/C$,[55] and taking $C \approx 0.9\times10^{-9}$ Pa^{-1} as the appropriate value for the stress-optical coefficient of PEO in water,[56] we can estimate the tension in the birefringent strand to be $\tau \approx \Delta\tau \approx 10^3$ Pa. Treating the strand as a stretched string in an inviscid medium pinned at the positions $x = \pm 15H$, such that $\Delta x = 3$ mm, we can estimate the first resonant frequency (n = 1 mode) we might expect for the strand:

$$f_n = \frac{n}{2\Delta x}\sqrt{\frac{\tau}{\rho'}}, \tag{3}$$

where the mass per unit length of the strand, $\rho' \approx 10^{-4}$ kg m^{-1}, is estimated from its width $\Delta y \approx 50$ μm, depth d = 2.1 mm and assuming the density of water. These apparently reasonable estimates result in an extremely high expected first resonant frequency of $f_1 \approx 0.5$ MHz. However, we have made a number of assumptions which would serve to moderate this value of f_1, if they could be well accounted for. Firstly, the ends of the strand are not rigidly clamped but are free to be displaced laterally. Secondly, the strand cannot be considered as a simple rate-independent elastic string but in reality is a viscoelastic liquid with some finite extensional viscosity on the order of $\eta_E = \Delta\tau/\dot{\varepsilon} \approx 2$ Pa s. In addition the added mass and viscosity of the surrounding fluid will further reduce the oscillation frequency. However, from this order of magnitude estimate for the fundamental frequency of the instability f_1 it appears that we would need to acquire images at a rate on the order of thousands of frames per second in order to exceed the Nyquist rate and properly resolve the oscillatory modes of the vibrating birefringent strand. The required frame rates can be achieved with certain specialized high speed CMOS cameras, however these have relatively low quantum efficiencies. Considering also the extremely short exposure times that would be required, we are doubtful that detection of time-resolved birefringence oscillations in dilute or semi-dilute polymer solutions is possible at the present time.

We also note that, strictly speaking from both a geometrical and a semantic standpoint, the "birefringent strand" we refer to is really a "birefringent sheet" since it occupies the *x*-*z* plane within the OSCER device. A more accurate analogy for the strand would thus be a taut ribbon rather than a taut string. Since the tension in the strand (or sheet) is maintained along the *x*-

direction only, this consideration should not complicate the preceding analysis. However, the analogy with a ribbon or sheet raises a second physical mechanism for the origin of the inertio-elastic instability; one that is similar to a flapping flag or sail in the wind.[57,58] The birefringent strand can be considered as an elastic sheet held under tension by shear stresses from the viscous fluid flowing past it. It is well known that above a critical flow velocity these conditions can give rise to regular sinuous motions of the sheet.[58] As the shearing stresses on the sheet increase at higher flow rates, these motions can become aperiodic and two-dimensional, as also appears to be the case in our experiment (Fig. 7).

V. CONCLUSIONS

We have used the recently-developed OSCER flow geometry, which generates an almost ideal planar homogenous elongational flow field along its symmetry planes, as a platform for the study of elastic flow instabilities in planar stagnation point flows. Aqueous polymer solutions with a wide range of rheological properties have been formulated and tested in the OSCER device over a wide range of imposed extension rates up to (and beyond) the onset of instability at a fluid-dependent critical flow rate $(\mathrm{Re}_{crit}, \mathrm{Wi}_{crit})$. Flow instabilities within the OSCER geometry have been characterized and classified based on the evolution of the flow-induced birefringent strands that can be imaged using an ABRIO polarizing microscope. Prior to the onset of instability, the birefringent strands are steady, symmetric and of uniform intensity along the outflowing symmetry axis of the OSCER device. Depending upon the value of the elasticity number at the critical conditions, $\mathrm{El}_{crit} = \mathrm{Wi}_{crit}/\mathrm{Re}_{crit}$, distinctive features are observed in the birefringence patterns that are imaged in the OSCER device after the onset of instability. For $\mathrm{El}_{crit} > 1$ the birefringent strand remains steady but becomes anti-symmetric, and is thus equivalent to the purely elastic symmetry-breaking flow bifurcations reported by Arratia *et al*.[30], Poole *et al*.[32] and others in the conventional cross-slot device. For $\mathrm{El}_{crit} < 1$ we observe an apparent broadening of the birefringent strand and a reduction in its intensity near the stagnation point. Space-time diagrams show that this flow is characterized by significant spatio-temporal fluctuations. We classify this as an inertio-elastic instability due to the important role of fluid inertia as well as fluid elasticity. The results presented in Table II and Fig. 13 indicate that the elasticity number of the fluid, defined as $\mathrm{El} = \mathrm{Wi}/\mathrm{Re} = 0.1\lambda\eta(\dot{\gamma})/\rho H D_h$, is the crucial

dimensionless parameter governing the nature of the instabilities that develop in planar stagnation point flows of polymer solutions.

More detailed observations of the inertio-elastic instability mode using one particular fluid (PEO2 in water) and a high speed (~O(100 fps)) birefringence imaging system, indicate that this mode of instability normally results in oscillations of the birefringent strand analogous to the first resonance mode on a stretched string or elastic sheet. This idea is supported by the occasional observation of a second inertio-elastic instability mode that is visually consistent with the second resonance mode of a stretched string or sheet. However, a rough estimate of the expected resonant frequency of the birefringent strand based on estimates of its length, mass per unit length and tension, indicate that much higher frame rate imaging (perhaps as high as thousands of frames per second) would be required in order to exceed the Nyquist aliasing frequency and thus achieve a quantitative measurement of the rate of vibration of the strand.

By plotting the onset conditions for instability in terms of the Weissenberg number and Reynolds number we have also mapped out the operating limits of the OSCER device as a planar extensional rheometer for viscoelastic polymer solutions. . This operating diagram can be viewed as a prototypical stability diagram for complex fluids in stagnation point extensional flows and spans a wide range of Wi-Re operating space. It may thus be a useful framework for guiding the formulation of fluids and the design of flow geometries suited for specific device applications as well as providing a useful benchmark comparison for validating numerical simulations of strong time-dependent and three-dimensional flows of complex fluids.

ACKNOWLEDGEMENTS

The authors acknowledge financial support from NASA Microgravity Fluid Sciences (Code UG) under grant NNX09AV99G. SJH also acknowledges the support of the European Commission under Marie Curie action FP7-PEOPLE-2011-IIF Grant No. 298220. We are indebted to Dr. J. A. Odell (University of Bristol) for the loan of optical apparatus used to perform high speed birefringence imaging and we thank Prof. M. A. Alves (Universidade do Porto) for helpful discussions and the use of laboratory facilities at CEFT.

[1] P.G. De Gennes, "Coil-stretch transition of dilute flexible polymers under ultrahigh velocity gradients," J. Chem. Phys. **60**, 5030-5042 (1974).

[2] E.J. Hinch, "Mechanical models of dilute polymer solutions for strong flows with large polymer deformations," Colloques Internationaux Du C.N.R.S. Polymeres Et Lubrification **233**, 241-247 (1974).

[3] R.G. Larson and J.J. Magda, "Coil-stretch transitions in mixed shear and extensional flows of dilute polymer solutions," Macromolecules **22**, 3004-3010 (1989).

[4] G.K. Batchelor, "Slender-body theory for particles of arbitrary cross-section in Stokes flow," J. Fluid Mech. **44**, 419-440 (1970).

[5] V. Tirtaatmadja and T. Sridhar, "A filament stretching device for measurement of extensional viscosity," J. Rheol. **37**, 1081-1102 (1993).

[6] S.J. Haward, J.A. Odell, Z. Li, and X.-F. Yuan, "Extensional rheology of dilute polymer solutions in oscillatory cross-slot flow: the transient behaviour of birefringent strands," Rheol. Acta **49**, 633-645 (2010).

[7] T. Sridhar, "An overview of the project M1," J. Non-Newtonian Fluid Mech. **35**, 85-92 (1990).

[8] S.J. Haward, M.S.N. Oliveira, M.A. Alves, and G.H. McKinley, "Optimized cross-slot flow geometry for microfluidic extensional rheometry," Phys. Rev. Lett. **109**, 128301 (2012).

[9] M.A. Alves, "Design of a cross-slot flow channel for extensional viscosity measurements," in *The XVth International Congress on Rheology, The Society of Rheology 80th Annual Meeting*, edited by A. Co, L.G. Leal, R.H. Colby, and A.J. Giacomm (American Institute of Physics, Monterey, 2008), pp. 240–242.

[10] M.S.N. Oliveira, S.J. Haward, G.H. McKinley, and M.A. Alves, "OSCER - an Optimized Shape Cross-slot Extensional Rheometer," To be submitted (2013).

[11] A. Keller and J.A. Odell, "The extensibility of macromolecules in solution; A new focus for macromolecular science," Colloid Polym. Sci. **263**, 181-201 (1985).

[12] J.A. Odell and A. Keller, "Fracture of isolated linear macromolecules in solution," J. Polym. Sci. Pol. Phys. **24**, 1889-1916 (1986).

[13] S.J. Haward and J.A. Odell, "Molecular orientation in non-Newtonian flow of dilute polymer solutions around spheres," Rheol. Acta **43**, 350-363 (2004).

[14] T.T. Perkins, D. E. Smith, and S. Chu, "Single polymer dynamics in an elongational flow," Science **276**, 2016-2021 (1997).

[15] D.E. Smith and S. Chu, "Response of Flexible Polymers to a Sudden Elongational Flow," Science **281**, 1335-1340 (1998).

[16] S.J. Haward, A. Jaishankar, M.S.N. Oliveira, M.A. Alves, and G.H. McKinley, "Extensional flow of hyaluronic acid solutions in an optimized microfluidic cross-slot device," Biomicrofluidics, Submitted (2013)

[17] F.J. Galindo-Rosales, M.A. Alves, and M.S.N. Oliveira, "Microdevices for extensional rheometry of low viscosity elastic liquids: a review," Microfluid. Nanofluid. **14**, 1-19 (2013)

[18] R.G. Larson, "Instabilities in viscoelastic flows," Rheol. Acta **31**, 213-263 (1992).

[19] S.J. Muller, "Elastically-influenced instabilities in Taylor-Couette and other flows with curved streamlines: a review," Korea-Aust. Rheol. J. **20**, 117-125 (2008).

[20] A. Groisman, M. Enzelberger, and S.R. Quake, "Microfluidic memory and control devices," Science **300**, 955-958 (2003).

[21] A. Groisman and S.R. Quake, "A microfluidic rectifier: anisotropic flow resistance at low Reynolds numbers," Phys. Rev. Lett. **92**, 094501 (2004).

[22] A. Groisman and V. Steinberg, "Efficient mixing at low Reynolds numbers using polymer additives," Nature **410**, 905-908 (2001).

[23] L.E. Rodd, T.P. Scott, D.V. Boger, J.J. Cooper-White, and G.H. McKinley, "The inertio-elastic planar entry flow of low-viscosity elastic fluids in micro-fabricated geometries," J. Non-Newtonian Fluid Mech. **129**, 1-22 (2005).

[24] L.E. Rodd, J.J. Cooper-White, D.V. Boger, and G.H. McKinley, "Role of the elasticity number in the entry flow of dilute polymer solutions in micro-fabricated contraction geometries," J. Non-Newtonian Fluid Mech. **143**, 170-191 (2007).

[25] S. Gulati, S.J. Muller, and D. Liepmann, "Direct measurements of viscoelastic flows of DNA in a 2:1 abrupt planar micro-contraction," J. Non-Newtonian Fluid Mech. **155**, 51-66 (2008).

[26] L.E. Rodd, D. Lee, K.H. Ahn, and J.J. Cooper-White, "The importance of downstream events in microfluidic viscoelastic entry flows: Consequences of increasing the constriction length," J. Non-Newtonian Fluid Mech. **165**, 1189-1203 (2010).

[27] Z. Li, X.-F. Yuan, S.J. Haward, J.A. Odell, and S. Yeates, "Non-linear dynamics of semi-dilute polydisperse polymer solutions in microfluidics: effects of flow geometry," Rheol. Acta **50**, 277-290 (2011).

[28] Z. Li, X.-F. Yuan, S.J. Haward, J.A. Odell, and S. Yeates, "Non-linear dynamics of semi-dilute polydisperse polymer solutions in microfluidics: A study of a benchmark flow problem," J. Non-Newtonian Fluid Mech. **166**, 951-963 (2011).

[29] A.M. Afonso, P.J. Oliveira, F.T. Pinho, and M.A. Alves, "Dynamics of high-Deborah-number entry flows: a numerical study," J. Fluid Mech. **677**, 272-304 (2011).

[30] P.E. Arratia, C.C. Thomas, J. Diorio, and J.P. Gollub, "Elastic instabilities of polymer solutions in cross-channel flow," Phys. Rev. Lett. **96**, 144502 (2006).

[31] J.A. Pathak and S.D. Hudson, "Rheo-optics of equilibrium polymer solutions: Wormlike micelles in elongational flow in a microfluidic cross-slot," Macromolecules **39**, 8782-8792 (2006).

[32] R.J. Poole, M.A. Alves, and P.J. Oliveira, "Purely elastic flow asymmetries," Phys. Rev. Lett. **99**, 164503 (2007).

[33] G.N. Rocha, R.J. Poole, M.A. Alves, and P.J. Oliveira, "On extensibility effects in the cross-slot flow bifurcation," J. Non-Newtonian Fluid Mech. **156**, 58-69 (2009).

[34] L. Xi and M.D. Graham, "A mechanism for oscillatory instability in viscoelastic cross-slot flow," J. Fluid Mech. **622**, 145-165 (2009).

[35] S.J. Haward, T.J. Ober, M.S.N. Oliveira, M.A. Alves, and G.H. McKinley, "Extensional rheology and elastic instabilities of a wormlike micellar solution in a microfluidic cross-slot device," Soft Matter **8**, 536-555 (2012).

[36] S.J. Haward and G.H. McKinley, "Stagnation point flow of wormlike micellar solutions in a microfluidic cross-slot device: Effects of surfactant concentration and ionic environment," Phys. Rev. E **85**, 031502 (2012).

[37] N. Dubash, P. Cheung, and A.Q. Shen, "Elastic instabilities in a microfluidic cross-slot flow of wormlike micellar solutions," Soft Matter **8**, 5847-5856 (2012).

[38] O.J. Harris and J.M. Rallison, "Instabilities of a stagnation point flow of a dilute polymer solution," J. Non-Newtonian Fluid Mech. **55**, 59-90 (1994).

[39] O.G. Harlen, J.M. Rallison, and M.D. Chilcott, "High-deborah-number polymer solutions flows of dilute polymer solutions," J. Non-Newtonian Fluid Mech. **34**, 319-349 (1990).

[40] O.G. Harlen, E.J. Hinch, and J.M. Rallison, "Birefringent pipes: the steady flow of a dilute polymer solution near a stagnation point," J. Non-Newtonian Fluid Mech. **44**, 229-265 (1992).

[41] A.J. Müller, J.A. Odell, and A. Keller, "Elongational flow and rheology of monodisperse polymers in solution," J. Non-Newtonian Fluid Mech. **30**, 99-118 (1988).

[42] S.P. Carrington and J.A. Odell, "How do polymers stretch in stagnation point extensional flow-fields?," J. Non-Newtonian Fluid Mech. **67**, 269-283 (1996).

[43] S.P. Carrington, J.P. Tatham, J.A. Odell, and A.E. Sáez, "Macromolecular dynamics in extensional flows: 1. Birefringence and viscometry," Polymer **38**, 4151-4164 (1997).

[44] C.J. Pipe, T.S. Majmudar, and G.H. McKinley, "High shear rate viscometry," Rheol. Acta **47**, 621-642 (2008).

[45] W.W. Graessley, "Polymer chain dimensions and the dependence of viscoelastic properties on concentration, molecular weight and solvent power," Polymer **21**, 258-262 (1980).

[46] K. Devanand and J.C. Selser, "Asymptotic behavior and long-range interactions in aqueous solutions of poly(ethylene oxide)," Macromolecules **24**, 5943-5947 (1991).

[47] H. Tadokoro, *Structure of Crystalline Polymers* (Krieger Publishing Company, Malabar, FL, 1990).

[48] S.L. Anna and G.H. McKinley, "Elasto-capillary thinning and breakup of model elastic liquids," J. Rheol. **45**, 115-138 (2001).

[49] M. Johnson, R. Kamm, C.R. Ethier, and T. Pedley, "Scaling laws and the effects of concentration polarization on the permeability of hyaluronic acid," Physicochem. Hydrodyn. **9**, 427-441 (1987).

[50] F. Meyer, D. Lohmann, and W.-M. Kulicke, "Determination of the viscoelastic behavior of sodium hyaluronate in phosphate buffered saline with rheo-mechanical and rheo-optical methods," J. Rheol. **53**, 799-818 (2009).

[51] A.Ö. Bingöl, D. Lohmann, K. Püschel, and W.-M. Kulicke, "Characterization and comparison of shear and extensional flow of sodium hyaluronate and human synovial fluid," Biorheology **47**, 205-224 (2010).

[52] M. Shribak and R. Oldenbourg, "Techniques for fast and sensitive measurements of two-dimensional birefringence distributions," Appl. Optics **42**, 3009-3017 (2003).

[53] C.L. Riddiford and H.G. Jerrard, "Limitations on the measurement of relaxation times using a pulsed Kerr effect method," J. Phys. D Appl. Phys. **3**, 1314-1321 (1970).

[54] S.J. Haward, V. Sharma, and J.A. Odell, "Extensional opto-rheometry with biofluids and ultra-dilute polymer solutions," Soft Matter **7**, 9908-9921 (2011).

[55] G.G. Fuller, *Optical Rheometry of Complex Fluids* (Oxford University Press, New York, 1995).

[56] Q. Zhang and L.A. Archer, "Optical polarimetry and mechanical rheometry of poly(ethylene oxide)-silica dispersions," Macromolecules **37**, 1928-1936 (2004).

[57] S. Taneda, "Waving motions of flags" J. Phys. Soc. Jpn. **24**, 392-401 (1968).

[58] M.J. Shelley and J. Zhang, "Flapping and bending bodies interacting with fluid flows" Annu. Rev. Fluid Mech. **43**, 449-465 (2011).

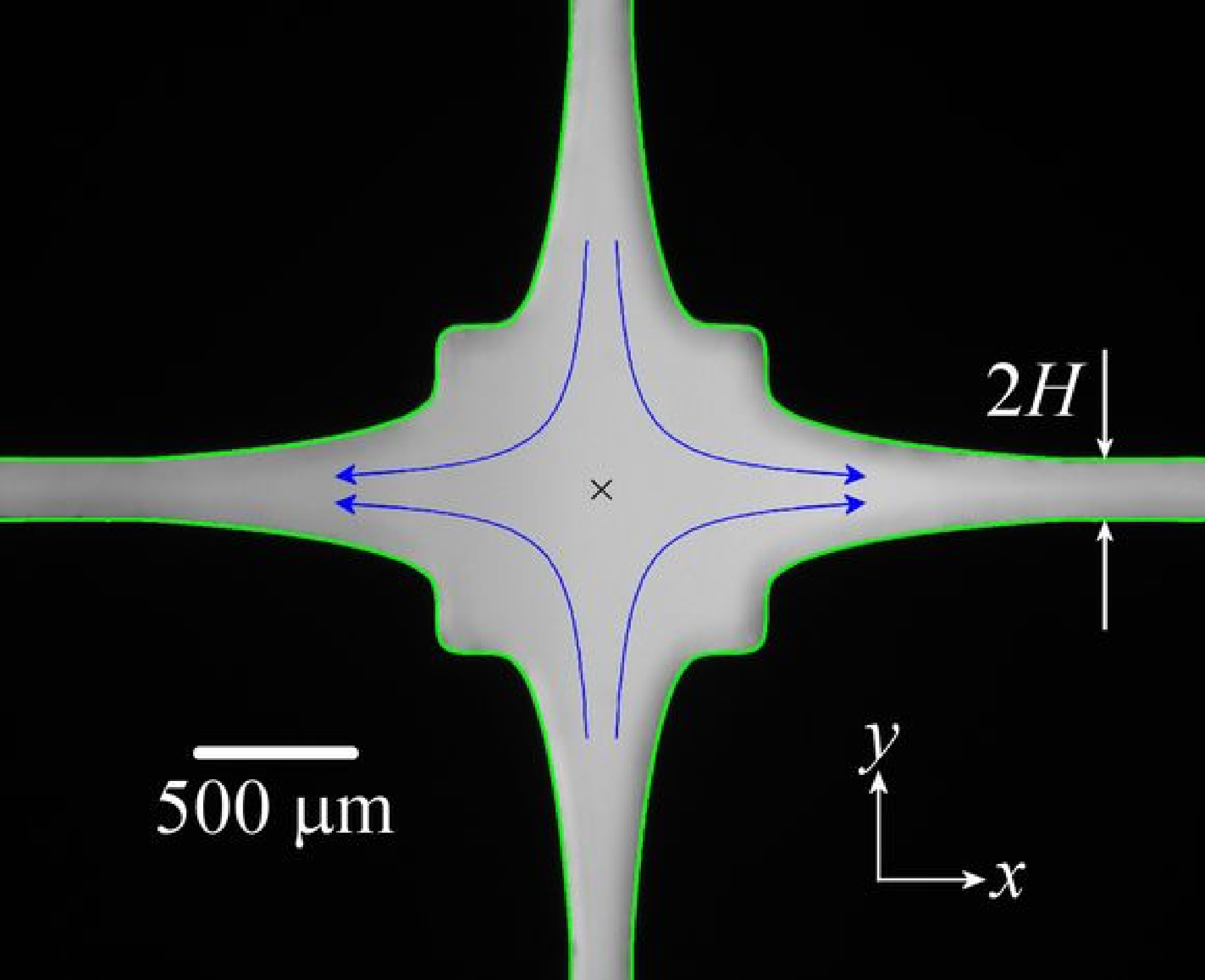
2H
500 μm
y
x

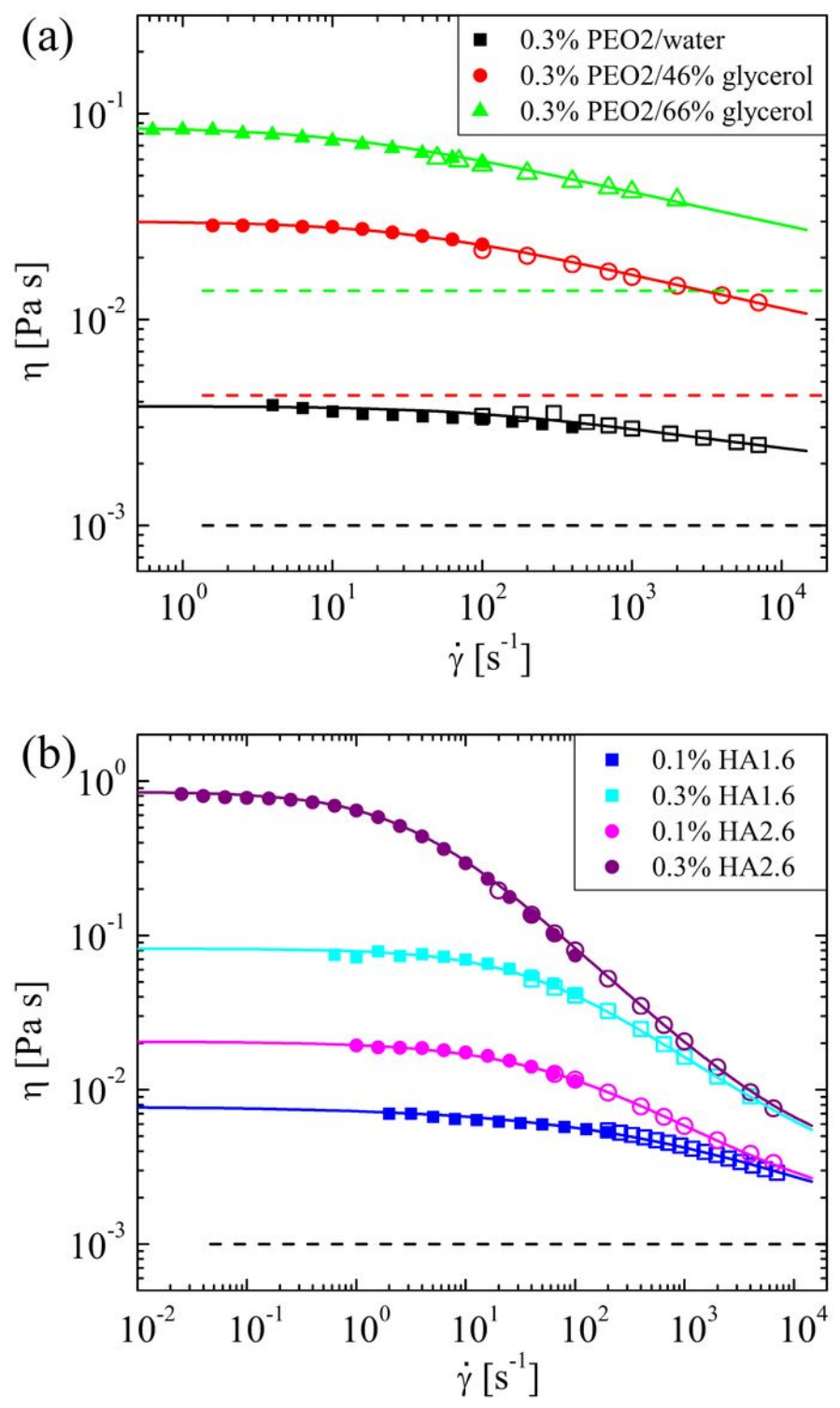
(a)
0.3% PEO2/water
0.3% PEO2/46% glycerol
0.3% PEO2/66% glycerol
η [Pa s]
$\dot{\gamma}$ [s^{-1}]
(b)
0.1% HA1.6
0.3% HA1.6
0.1% HA2.6
0.3% HA2.6
η [Pa s]
$\dot{\gamma}$ [s^{-1}]

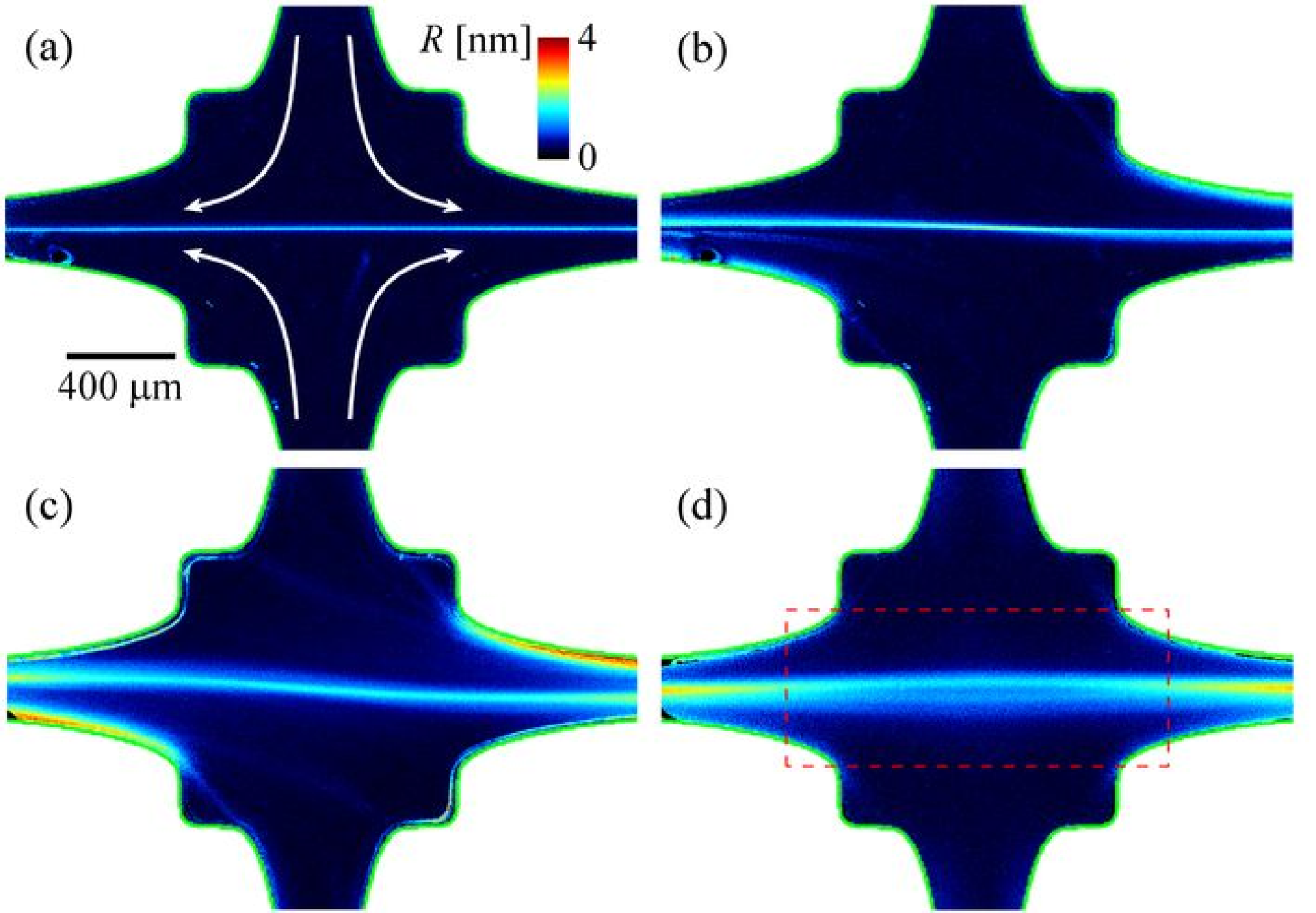
(a)
R [nm]
4
0
400 μm
(b)
(c)
(d)

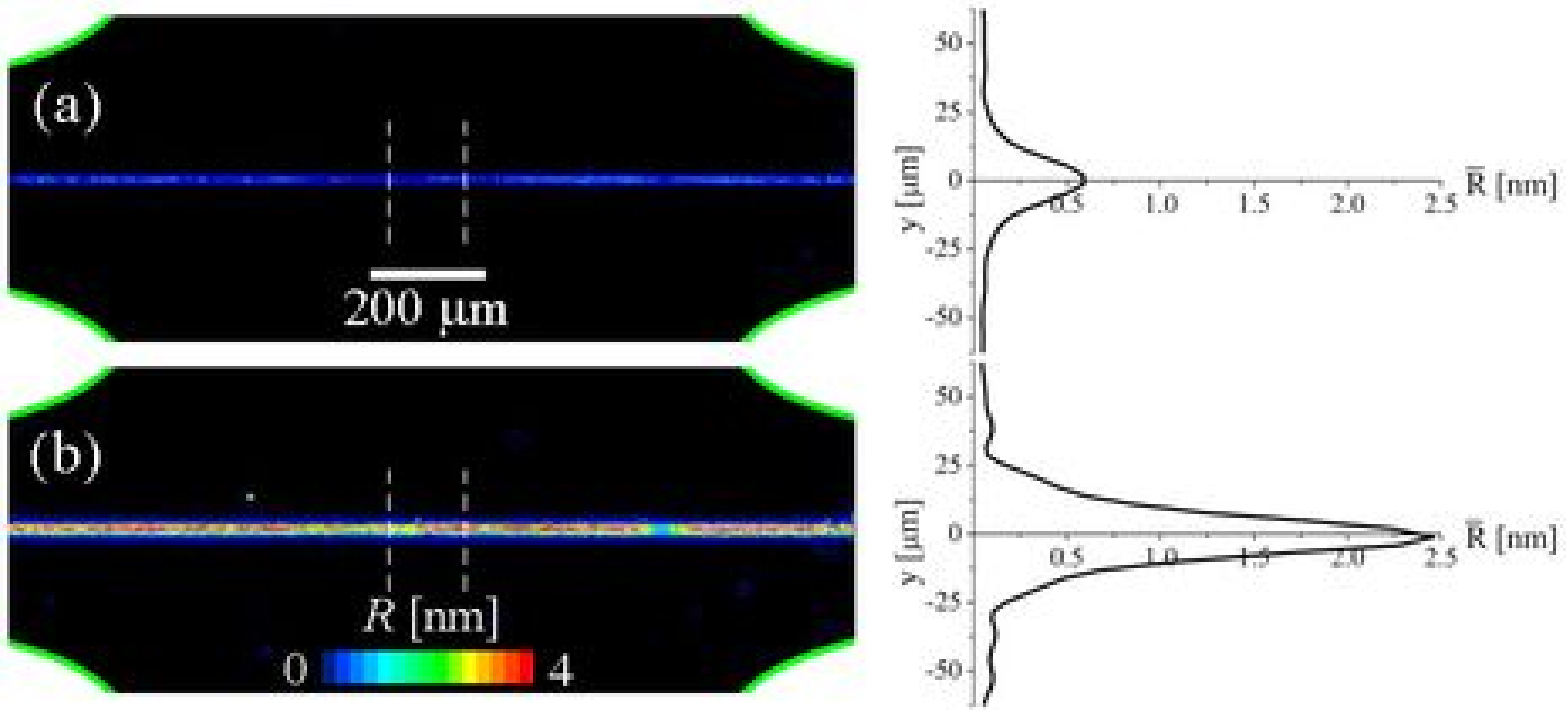
(a)
200 μm
(b)
R [nm]
0
4
50
25
0
-25
-50
y [μm]
0.5
1.0
1.5
2.0
2.5
R̄ [nm]

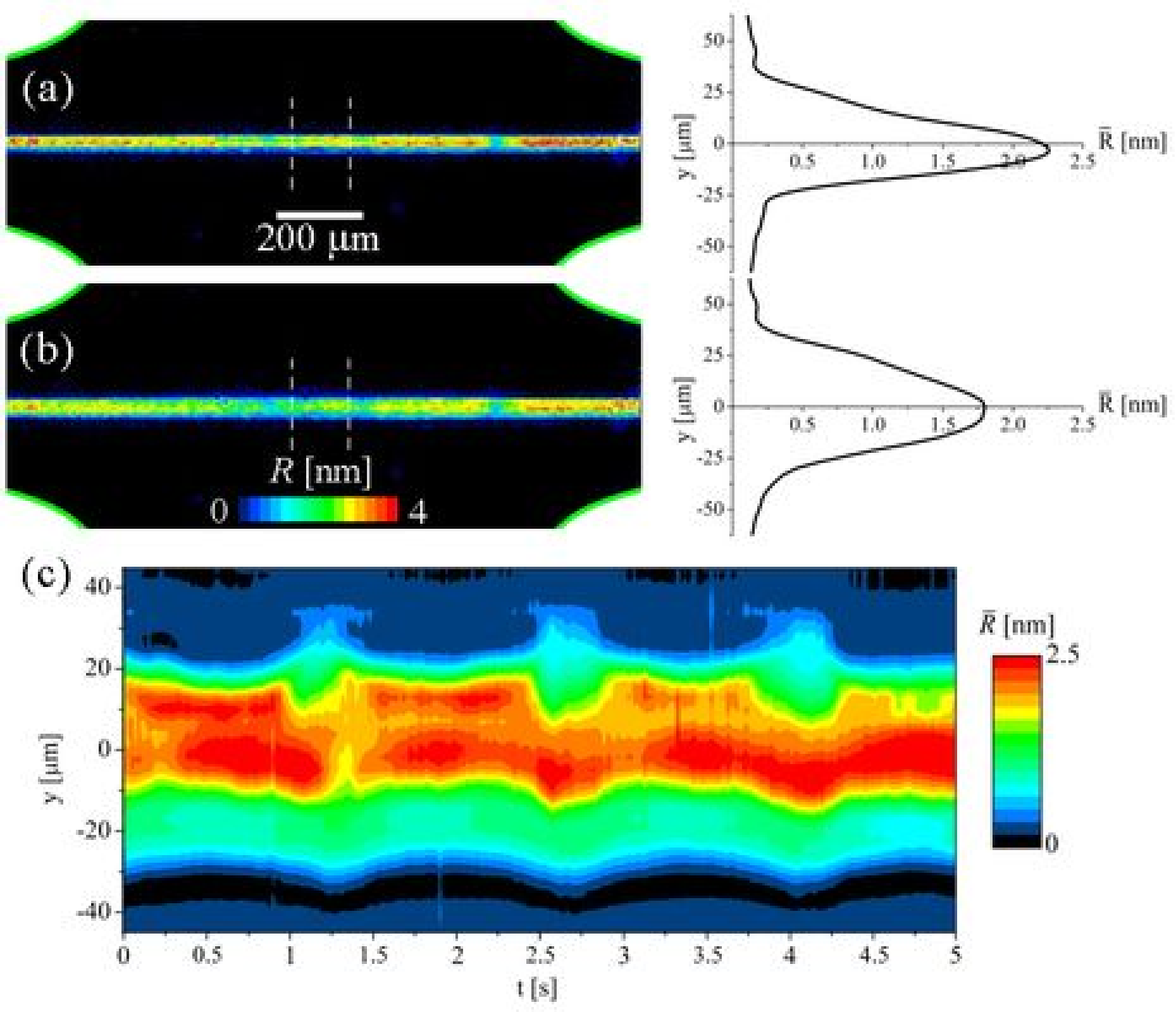
(a)
200 μm
(b)
R [nm]
0
4
y [μm]
R̄ [nm]
(c)
y [μm]
t [s]
R̄ [nm]
2.5
0

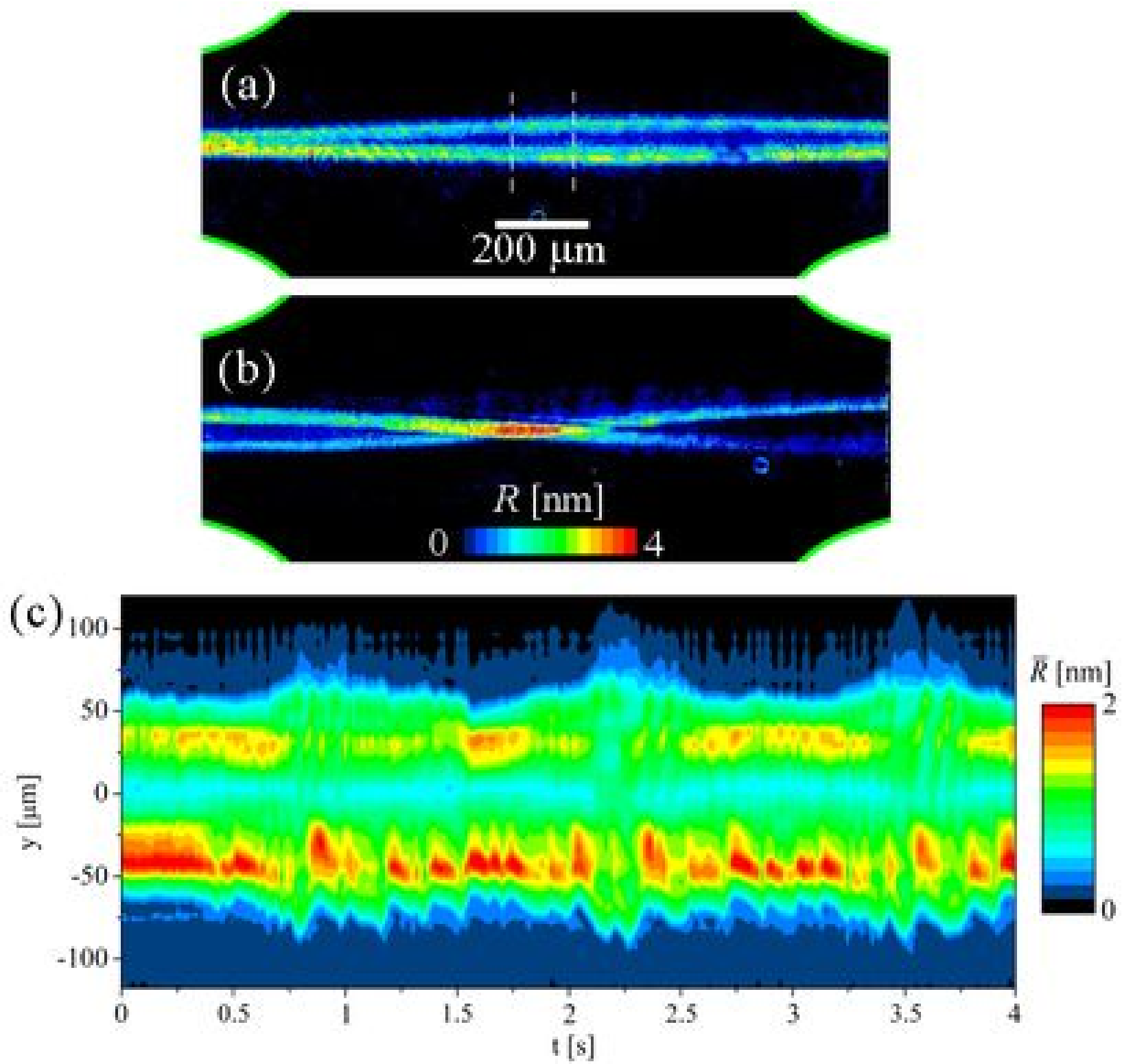
(a)
200 µm
(b)
R [nm]
0
4
(c)
100
50
0
-50
-100
y [µm]
0
0.5
1
1.5
2
2.5
3
3.5
4
t [s]
R̄ [nm]
2
0

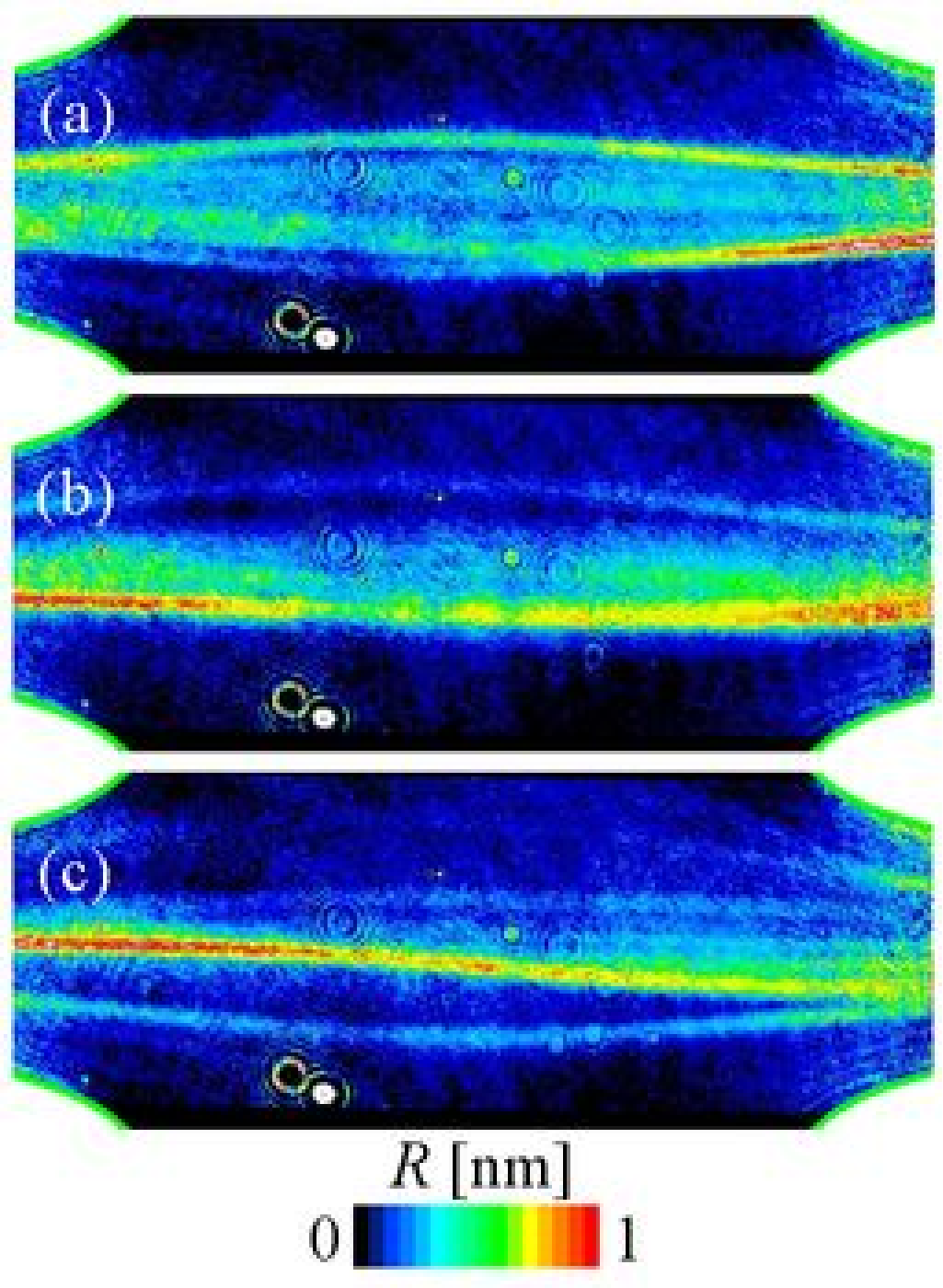
(a)
(b)
(c)
R [nm]
0
1

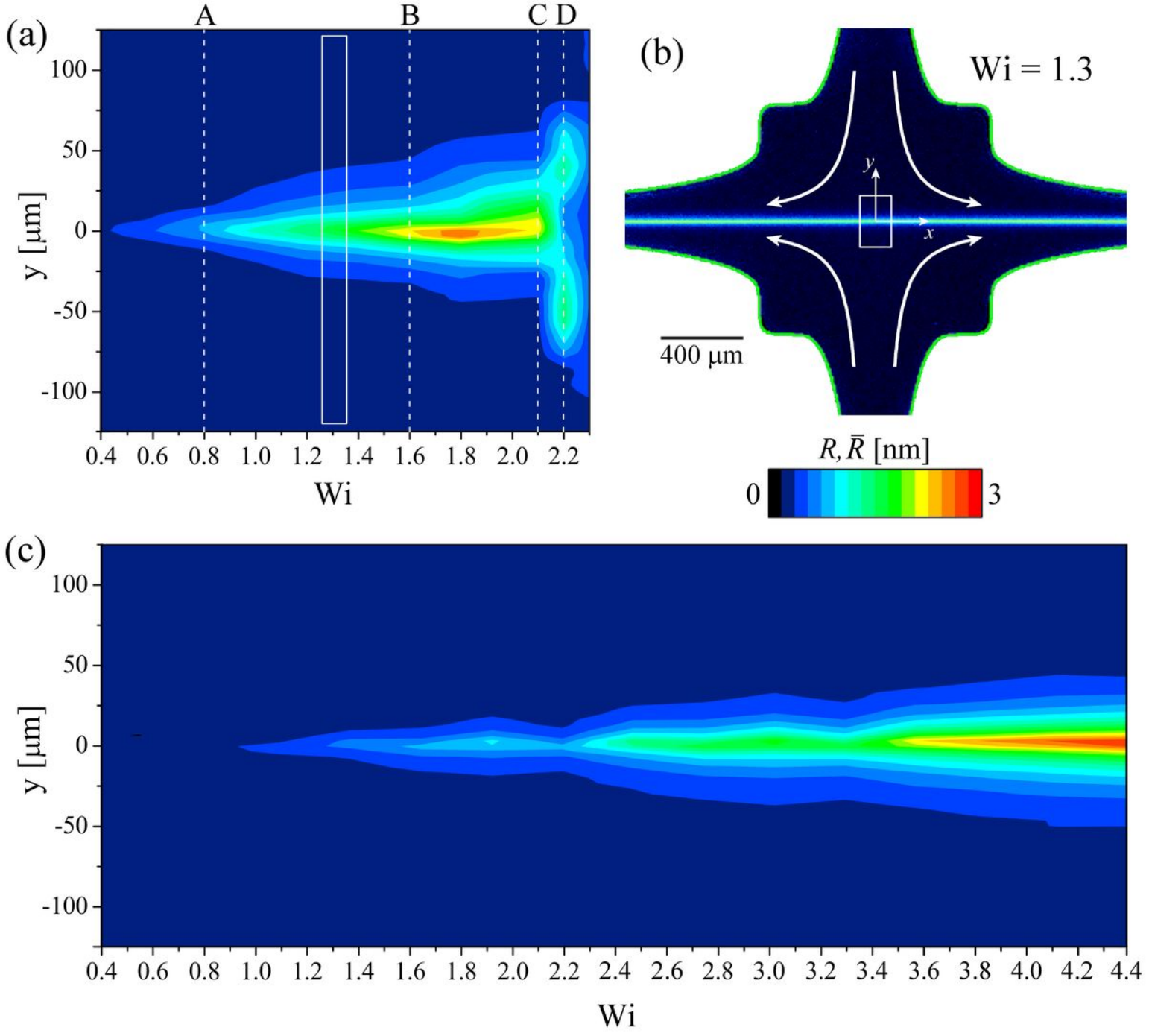
(a)
A
B
C D
100
50
0
-50
-100
y [μm]
0.4 0.6 0.8 1.0 1.2 1.4 1.6 1.8 2.0 2.2
Wi
(b)
Wi = 1.3
y
x
400 μm
R, R̄ [nm]
0
3
(c)
100
50
0
-50
-100
y [μm]
0.4 0.6 0.8 1.0 1.2 1.4 1.6 1.8 2.0 2.2 2.4 2.6 2.8 3.0 3.2 3.4 3.6 3.8 4.0 4.2 4.4
Wi

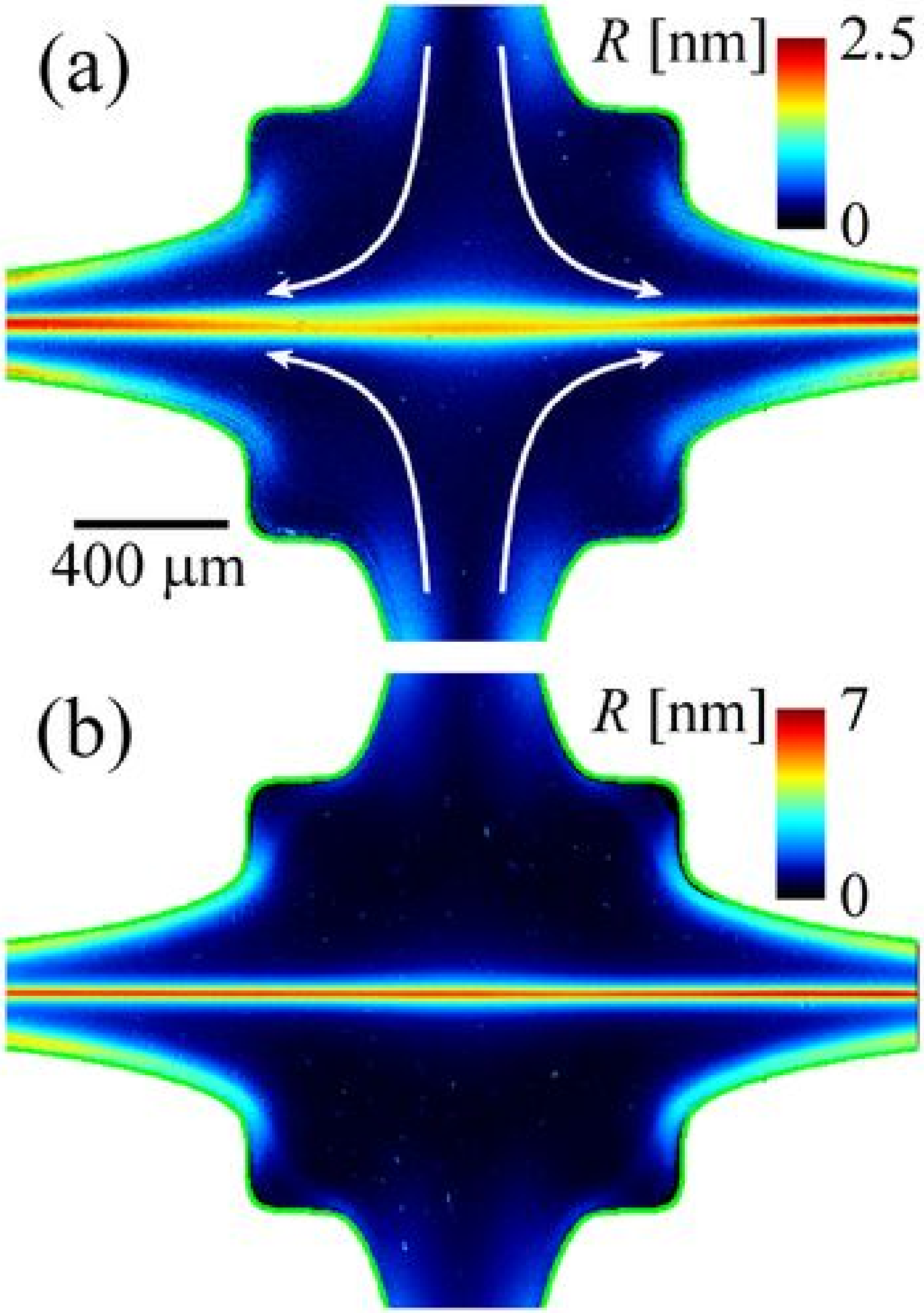
(a)
R [nm]
2.5
0
400 μm
(b)
R [nm]
7
0

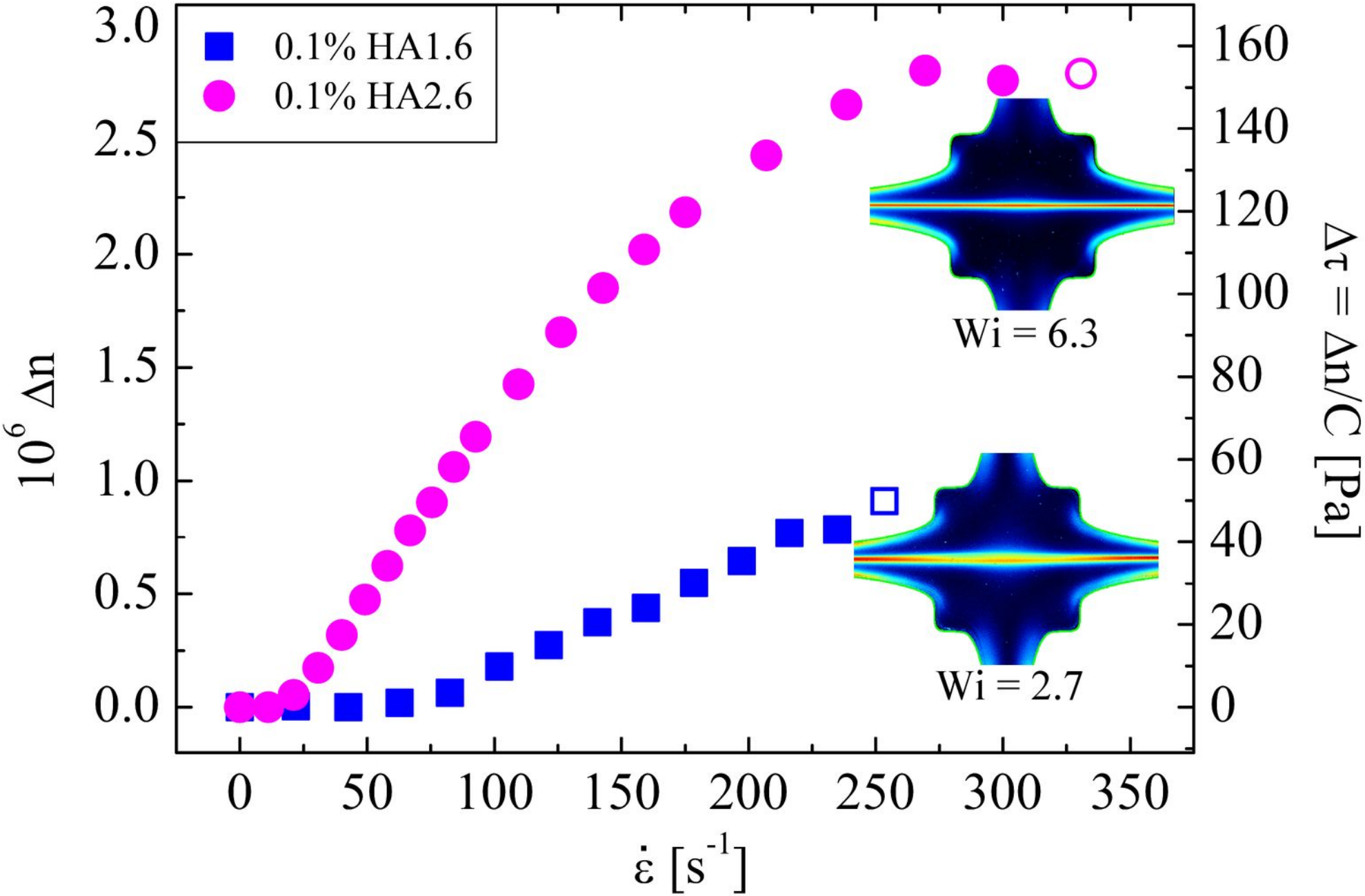
0.1% HA1.6
0.1% HA2.6
Wi = 6.3
Wi = 2.7
$10^6\,\Delta n$
$\Delta\tau = \Delta n/C$ [Pa]
$\dot{\varepsilon}$ [s^{-1}]
0.0
0.5
1.0
1.5
2.0
2.5
3.0
0
20
40
60
80
100
120
140
160
0
50
100
150
200
250
300
350

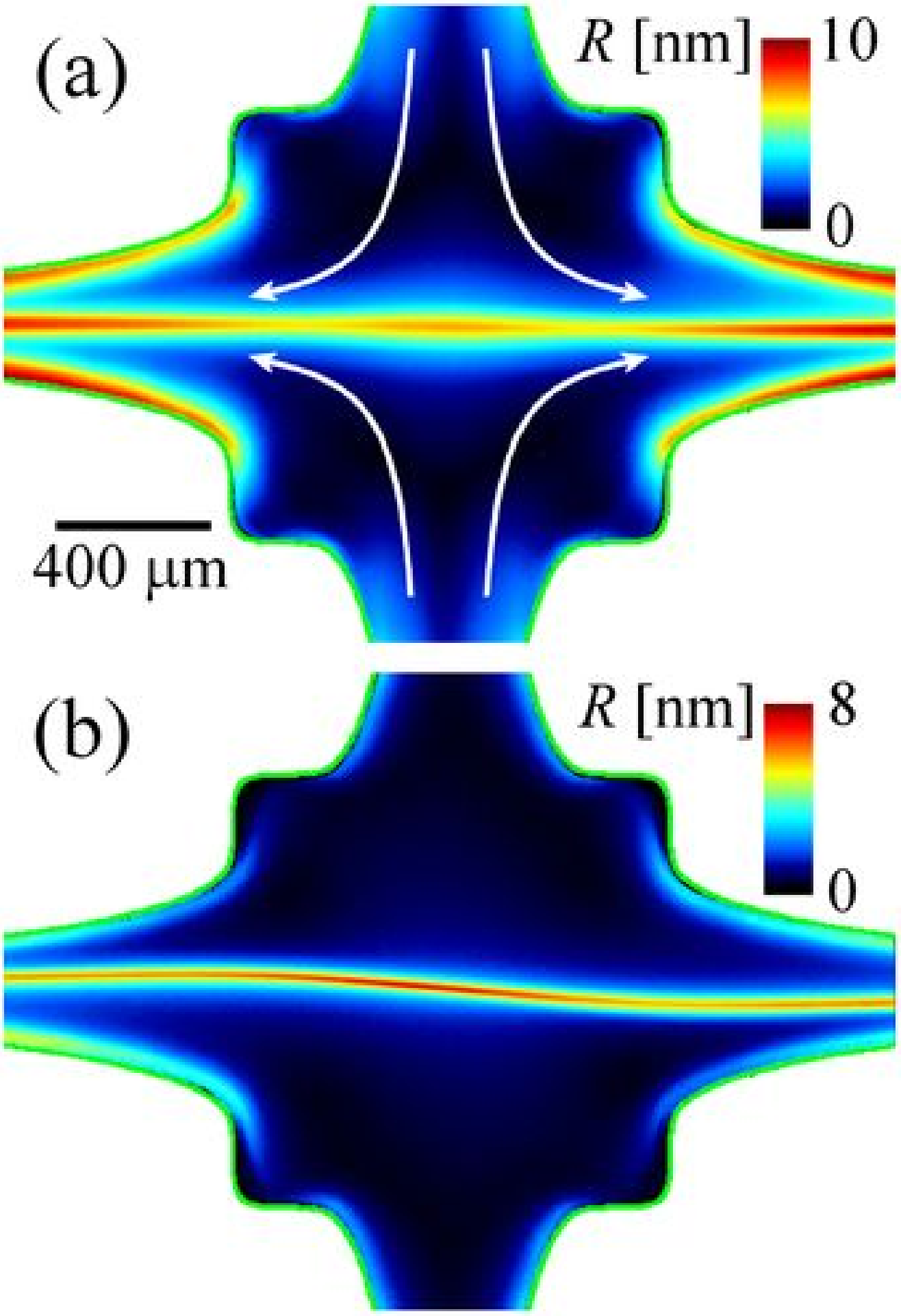
(a)
R [nm]
10
0
400 μm
(b)
R [nm]
8
0

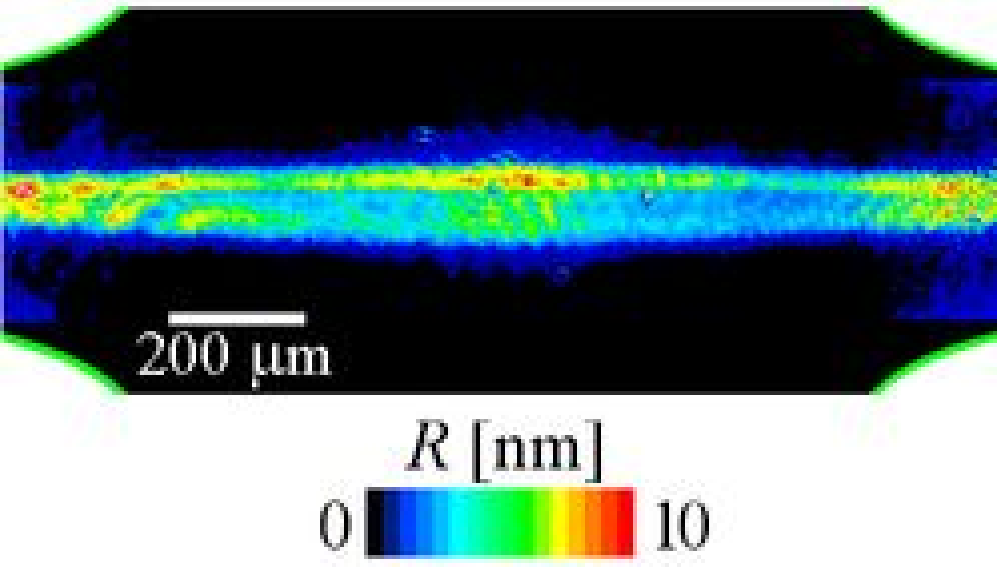
200 μm
R [nm]
0
10

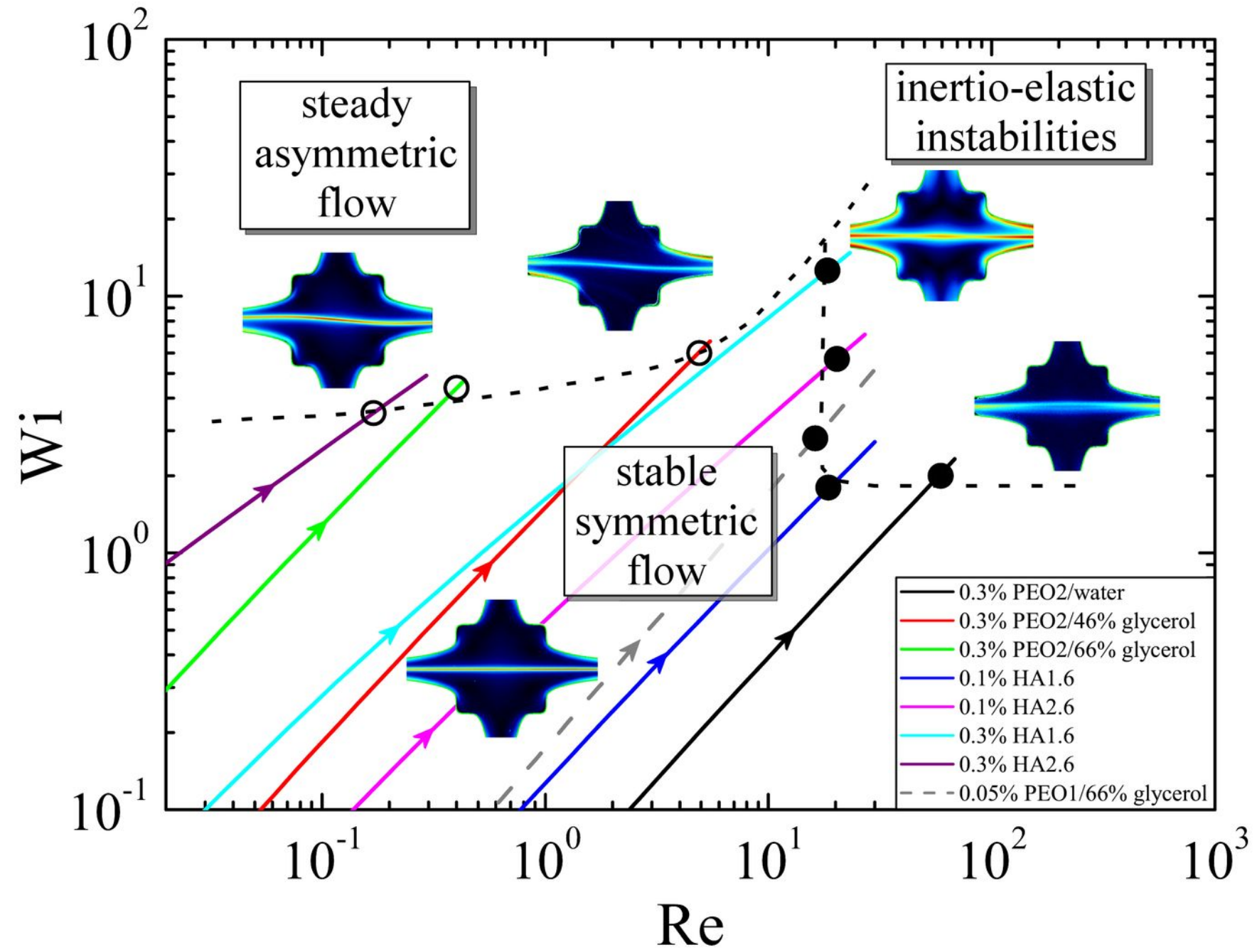
steady
asymmetric
flow
inertio-elastic
instabilities
stable
symmetric
flow
0.3% PEO2/water
0.3% PEO2/46% glycerol
0.3% PEO2/66% glycerol
0.1% HA1.6
0.1% HA2.6
0.3% HA1.6
0.3% HA2.6
0.05% PEO1/66% glycerol
Wi
Re
10^{2}
10^{1}
10^{0}
10^{-1}
10^{-1}
10^{0}
10^{1}
10^{2}
10^{3}